The Astrophysical Journal, 677:630–656, 2008 April 10

THE COMPLETE CENSUS OF 70 μm–BRIGHT DEBRIS DISKS WITHIN "THE FORMATION AND EVOLUTION OF PLANETARY SYSTEMS" *SPITZER* LEGACY SURVEY OF SUN-LIKE STARS

Lynne A. Hillenbrand,[1] John M. Carpenter,[1] Jinyoung Serena Kim,[2] Michael R. Meyer,[2] Dana E. Backman,[3] Amaya Moro-Martín,[4] David J. Hollenbach,[5] Dean C. Hines,[6] Ilaria Pascucci,[2] and Jeroen Bouwman[7]

Received 2007 September 3; accepted 2007 December 22

ABSTRACT

We report detection of cool dust surrounding solar-type stars from observations performed as part of the *Spitzer* Legacy Science Program FEPS. From a sample of 328 stars having ages ~0.003–3 Gyr we have selected sources with 70 μm flux densities indicating excess in their SEDs above expected photospheric emission. Six strong excess sources are likely primordial circumstellar disks, remnants of the star formation process. Another 25 sources having $\geq 3\,\sigma$ excesses are associated with dusty debris disks, generated by collisions within planetesimal belts that are possibly stirred by existing planets. Six additional sources with $\geq 2\,\sigma$ excesses require confirmation as debris disks. In our analysis, most (>80%) 70 μm excess sources have $\geq 3\,\sigma$ excesses at 33 μm as well, while only a minority (<40%) have $\geq 3\,\sigma$ excesses at 24 μm. The rising SEDs toward (and perhaps beyond) 70 μm imply dust temperatures <45–85 K for debris in equilibrium with the stellar radiation field. From fitted single-temperature blackbody models we infer bulk dust properties such as characteristic temperature, location, fractional luminosity, and mass. For $>\frac{1}{3}$ of the debris sources we find that multiple temperature components are suggested, implying a dust distribution extending over many tens of AU. Because the disks are dominated by collisional processes, the parent body (planetesimal) belts may be extended as well. Preliminary assessment of the statistics of cold debris around Sun-like stars shows that ~10% of FEPS targets with masses between 0.6 and 1.8 $M_\odot$ and ages between 30 Myr and 3 Gyr exhibit excess 70 μm emission. We find that fractional excess amplitudes appear higher for younger stars and that there may be a trend in 70 μm excess frequency with stellar mass.

Subject headings: circumstellar matter — infrared: general — Kuiper Belt — planetary systems — stars: individual (HD 104860, HD 105, HD 107146, HD 122652, HD 141943, HD 14306, HD 145229, HD 150706, HD 17925, HD 187897, HD 191089, HD 201219, HD 202917, HD 204277, HD 206374, HD 209253, HD 219498, HD 22179, HD 25457, HD 31392, HD 35850, HD 37484, HD 377, HD 38207, HD 38529, HD 61005, HD 6963, HD 70573, HD 72905, HD 85301, HD 8907 MML 17, PDS 66, [PZ99] J161411.0−230536, RX J1111.7−7620, RX J1842.9−3532, RX J1852.3−3700)

Online material: color figures

1. INTRODUCTION

Revolutionary improvements in astronomical observing capability are directed not only toward the distant reaches of the universe, but also to our nearest neighbors beyond, and even within, the solar system. In exploiting these new capabilities, we scrutinize old paradigms in new detail. The *Spitzer Space Telescope* is no exception, and a major science area for *Spitzer* has been the investigation of dusty circumstellar disks: both young primordial and older debris systems. *Spitzer* has unprecedented ability to detect the Rayleigh-Jeans tail of stellar photospheres in the 3–70 μm mid-infrared regime, and hence small excesses above those photospheres due to circumstellar dust; for sizable samples of nearby stars, the photometric accuracy is dominated by calibration uncertainty rather than by signal-to-noise ratio (S/N) considerations. *Spitzer* has thus extended our knowledge of disks beyond the brightest/nearest objects of various classes, to previously unexplored realms of completeness in, e.g., volume, spectral type, and age. In particular, *Spitzer* has enabled statistically significant surveys for warm ($T_{\rm dust} \sim 125$–300 K) dust in the outer terrestrial zone ($R_{\rm dust} \sim 1$–5 AU) and cold ($T_{\rm dust} < 40$–120 K) dust in the Jovian/Kuiper zone ($R_{\rm dust} > 5$–50 AU) of potential solar system analogs having a wide range of ages.

The current Kuiper Belt dust mass is estimated at $\approx 1 \times 10^{-5}\,M_\oplus$ in subcentimeter-sized particles, based on several different measures such as *IRAS* and *COBE* upper limits to cold emission in the ecliptic plane and associated modeling (e.g., Backman et al. 1995; Teplitz et al. 1999) of assumed 2–5000 μm grains, or detections of outer solar system dust thought to originate from the Kuiper Belt (Landgraf et al. 2002) and the dynamical model of Moro-Martin & Malhotra (2003) for ~1–150 μm grains. There is currently an additional $M \approx 0.1\,M_\oplus$ in large (more than centimeter sized) bodies (Gladman et al. 2001). Although the numbers are uncertain by probably 1–1.5 orders of magnitude, the above may be compared to an inferred $M \approx 1 \times 10^{-3}\,M_\oplus$ in dust and 10–50 $M_\oplus$ for the large bodies during the early debris stages at a few tens of Myr (Stern & Colwell 1997; Stern 1996b). This dust level is easily detected by *Spitzer* for nearby solar-type stars. In contrast, the low dust mass observed at the current solar age is not detectable.

The *Spitzer* Legacy program FEPS (Formation and Evolution of Planetary Systems) was designed to study the final stages of primordial disk dissipation and the development and evolution of debris disks around solar-mass stars over a range of ages. The *Spitzer* data include IRAC and MIPS photometry and IRS

[1] Astrophysics, California Institute of Technology, Pasadena, CA 91125.
[2] Steward Observatory, University of Arizona, Tucson, AZ 85721.
[3] SOFIA/SETI Institute, Mountain View, CA 94043.
[4] Astrophysics, Princeton University, Princeton, NJ 08540.
[5] NASA/Ames Research Center, Moffett Field, CA 94035.
[6] Space Science Institute, Boulder, CO 80301.
[7] Max-Planck-Institut für Astronomie, D-69117 Heidelberg, Germany.

spectrophotometry for 328 sources. Approximately 55 stars in each of 6 logarithmic age bins between 3 Myr and 3 Gyr of age were observed for the FEPS program. The targets span a narrow mass range (95% are within 0.8–1.5 $M_{\odot}$) in order to focus on Sun-like stars. The targets are proximate enough ($d \approx 10$–200 pc) to enable a complete census for circumstellar dust comparable in quantity to predictions from simple models of our solar system's collisional evolution as a function of stellar age (such as that discussed in Meyer et al. 2007). Sensitivity was further maximized by choosing targets in regions of lower infrared background over those of the same age in regions of higher background/cirrus. A value of S/N > 30 is obtained on the underlying stellar photosphere at 3.6, 4.5, 8, and 24 μm with IRAC and MIPS photometric observations, while S/N > 4 is achieved out to 35 μm from IRS spectrophotometric observations for >90% of the objects.

The main aim of FEPS is to trace dust evolution via spectral energy distribution (SED) interpretation and thereby to probe the detritus indicative of planet formation and evolution. In this contribution we focus on sources that are detected at 70 μm with flux densities in excess of those expected from the stellar photosphere. Six such FEPS objects (RX J1852.3−3700; HD 143006; RX J1842.9−3532; 1RXS J132207.2−693812, aka PDS 66; RX J1111.7−7620; and 1RXS J161410.6−230542, aka [PZ99] J161411.0−230536) are considered "primordial disks" and have been presented also by Silverstone et al. (2006) and Bouwman et al. (2008). These young disks have strong excess emission not only at 70 μm but also shortward, down to at least 3–8 μm. We provide their data again here, for completeness and for context. However, our main focus is on the larger sample of "debris disks," which generally have weaker excess emission at 70 μm, 24–33 μm flux densities consistent with, or only moderately in excess of, expected photospheric values, and <3–13 μm flux densities that are purely photospheric. Our debris sample includes 25 sources with >3 σ significant and six possible sources with 2–3 σ significant cold disk systems detected at 70 μm. Of the total, 14 are newly appreciated debris disk systems announced here, while the remainder have been reported previously, including in FEPS contributions by Meyer et al. (2004), Kim et al. (2005), and Pascucci et al. (2006); see Table 1 for details.

We begin with a description of the *Spitzer* observations and data handling (§ 2). We then present our methods for distinguishing detections from noise at 70 μm and our results in the form of color-color diagrams, excess S/N histograms, and SEDs that demonstrate the existence of 70 μm excesses indicative of cool circumstellar material (§ 3). We proceed to analyze the SEDs in terms of single-temperature blackbody models and argue that in $\gtrsim\frac{1}{3}$ of the cases multitemperature models indicative of a range of dust radii are a better match to the data than are the narrow rings implied by single-temperature models (§ 4). Our modeling results indicate dust temperatures typically <85 K, which imply, depending on the stellar parameters, corresponding dust inner radii of typically 5–50 AU and (poorly constrained) dust outer radii of typically several hundred AU. Comparison (§ 5) with inferred parent star ages of the theoretical timescales for dust depletion mechanisms, such as inward drag due to Poynting-Robertson (P-R) or corpuscular effects, outward push due to stellar radiative or mechanical effects, and in situ collisional destruction, suggests that the dust is continuously generated debris resulting from collisions among an unseen population of planetesimals. Planetesimal orbits can be perturbed either by the largest embryos in the planetesimal population or by planetary mass bodies, generating in both cases a steady state collisional cascade. Alternately, debris dust may be the result of individual, large catastrophic collisions that artificially raise the mass in small dust particles over steady state evolution values. Trends in debris disk detections with stellar age and mass are investigated (§ 6). Finally, we place our results into a larger context in § 7 and then conclude in § 8.

2. SAMPLE, OBSERVATIONS, AND DATA PROCESSING

The FEPS program utilized all three *Spitzer* science instruments, IRAC, IRS, and MIPS, to observe 328 solar-type stars. Meyer et al. (2006) provide a description of the FEPS observing strategy. Among the FEPS sample are 15 previously suspected (based on *IRAS* or *ISO* literature) debris or long-lived primordial disk systems. Ten of these 15 were observed by FEPS for the purpose of probing primordial gas disk dissipation (e.g., Pascucci et al. 2006, 2007), while the others were either serendipitously on our lists or suggested as excess sources after the FEPS program was submitted. The sources selected ab initio because they were claimed to exhibit infrared excess emission (only 11 of which are in fact confirmed by *Spitzer*) cannot be included in statistical analyses of FEPS *Spitzer* data for debris characteristics as a function of stellar age, stellar mass, stellar metallicity, stellar rotation, etc. However, we do include them in this paper, which presents disk detections and simple dust models.

J. M. Carpenter et al. (2008b, in preparation) provide a detailed discussion of realized FEPS observation, data reduction, and data validation procedures. We review here only those details of particular relevance to the present discussion of 70 μm excess. Four sources, HD 17925, HD 72905, HD 202917, and HD 216803, were observed at 70 μm not by FEPS but instead by the GTO program described by Bryden et al. (2006), who employ the same observing strategy as is standard for FEPS; the data were obtained from the *Spitzer* archive and processed using standard FEPS techniques. These particular sources were included in FEPS for the purpose of the gas disk dissipation experiment discussed above. MIPS 160 μm photometry was obtained by the FEPS project for a subsample of the full target list. It derives for most of the sources discussed here from follow-up *Spitzer* GO-2 and GO-3 programs in which additional 160 μm data[8] were obtained for FEPS sources with detected 70 (and/or 33) μm excesses.

Exposure times at 70 μm were 10 s per data collection event or image, with eight images taken per cycle. The number of cycles varied between (1, for the four GTO targets) 2 and 14 in order to reach the desired depth. Our original intent to detect photospheres at 70 μm was predicated on prelaunch sensitivity estimates. However, the higher than expected rate of large cosmic-ray hits reduced the on-orbit sensitivity by about a factor of 3 (Rieke et al. 2004), so we attempted instead for each of our targets to reach a common sensitivity relative to an estimate for the outer solar system dust level at the age of the star (see § 3.1).

Spitzer data were processed initially by the *Spitzer* Science Center pipeline S13. Postpipeline processing of IRAC, IRS, and MIPS data, including further reduction details, photometry/spectral extraction, error derivation, and flux density calibration discussions, is given in J. M. Carpenter et al. (2008b, in preparation);

[8] MIPS 160 μm data from GO-2 and GO-3 followed the standard FEPS observations, using 10 s exposure time per data collection event with 2–4 cycles (typically 4). Raw data were processed with SSC pipeline S14.4.0 and the MIPS DAT pipeline (Gordon et al. 2005) ver. 3.02. The final mosaic image has 8″ pixel^{-1}. The flux conversion factor from instrumental units to MJy sr^{-1} is 44.7, and the absolute calibration uncertainty is 12% (http://ssc.spitzer.caltech.edu/mips/calib/conversion.html). For aperture photometry we used an aperture radius of 24″, a sky annulus spanning 64″–128″, and an aperture correction of 2.380. Uncertainty was calculated by propagating the measured rms deviation in the sky area over the source aperture.

TABLE 1

STELLAR PROPERTIES

Source	d (pc)	log (age/yr)	Spectral Type	$T_{\rm eff}$ (K)	log ($L/L_{\odot}$)	MIR Excess References	Comment
Tier 1 Debris Disks (Excess S/N$_{70\,\mu m} \geq 3$)							
HD 105	40	7.5	G0 V	5948	0.12	1, 2	
HD 377	40	7.5	G2 V	5852	0.09	3	FEPS excess discovery
HD 6963	27	9.0	G7 V	5517	−0.26	4	FEPS excess discovery
HD 8907[a]	34	8.5	F8	6250	0.32	1, 4	
HD 22179	100	8.0	G5 IV	5986	0.36	3	FEPS excess discovery
HD 25457[a]	19	8.0	F7 V	6172	0.32	1	
HD 31392	26	9.0	K0 V	5357	−0.26	3	FEPS excess discovery
HD 35850[a]	27	7.5	F7/8 V	6047	0.25	1	
HD 37484[a]	60	8.0	F3 V	6656	0.55	5, 6	
HD 38207[a]	127	8.0	F2 V	6769	0.72	1	
HD 38529	42	9.5	G8 III/IV	5361	0.82	3, 7	FEPS excess discovery
HD 61005	35	8.0	G3/5 V	5456	−0.25	3	FEPS excess discovery
HD 72905[a,b]	14	8.0	G1.5	5831	−0.04	6	
HD 85301	32	9.0	G5	5605	−0.15	3	FEPS excess discovery
HD 104860	48	7.5	F8	5950	0.12	3	FEPS excess discovery
HD 107146	29	8.0	G2 V	5859	0.04	8, 9	FEPS precursor work
HD 122652	37	9.5	F8	6157	0.18	4	FEPS excess discovery
HD 145229	33	9.0	G0	5893	−0.02	4	FEPS excess discovery
HD 150706	27	9.0	G3 (V)	5883	−0.02	2	FEPS excess discovery
HD 187897	33	9.0	G5	5875	0.10	3	FEPS excess discovery
HD 191089[a]	54	8.5	F5 V	6441	0.50	10	
HD 201219[c]	36	9.0	G5	5604	−0.16	3	FEPS excess discovery; small positional offset
HD 202917[a,b]	46	7.5	G5	5553	−0.18	1	
HD 209253[a]	30	8.0	F6/7 V	6217	0.21	1	
HD 219498	150	8.5	G5	5671	0.69	3	FEPS excess discovery
Tier 2 Debris Disks (Excess S/N$_{70\,\mu m} \geq 2$ and <3)							
HD 17925[a,b]	10	8.0	K1 V	5118	−0.43	11	
HD 70573	46	8.0	G1/2 V	5841	−0.23	3	Moderate positional offset
HD 141943	67	7.5	G0/2 V	5805	0.43	3	Moderate positional offset; excess detected with IRS
HD 204277	34	8.5	F8	6190	0.29	3	Small positional offset
HD 206374	27	9.0	G6.5	5580	−0.17	4	FEPS excess discovery; moderate positional offset
MML 17	124	7.0	G0 IV	6000	0.43	3	Some concern upon visual inspection
Primordial Disks							
HD 143006[a]	145	6.5	G6/8	5884	0.39	12	
PDS 66	86	7.0	K1 IVe	5228	0.10	13	
[PZ99] J161411.0−230536	145	6.5	K0	4963	0.50	14	
RX J1111.7−7620[c]	153	6.5	K1	4621	0.21	6	
RX J1842.9−3532	130	6.5	K2	4995	−0.01	15	
RX J1852.3−3700	130	6.5	K3	4759	−0.23	15	
Unconfirmed Debris Disks Suggested in Previous Literature							
HD 41700 [a]	27	8.0	F8/G0 V	6140	0.24	16	Undetected by FEPS but 2.9 σ 70 μm source in GO-2 program
HD 104467 [c]	118	6.5	G5 III/IV	5690	0.75	3[d]	70 μm source is offset by 12.8″ and likely unassociated
HD 134319 [a]	44	8.0	G5	5656	−0.14	1	
HD 216803 [a,b]	7.6	8.5	K4	4625	−0.71	17	
ScoPMS 214	145	6.5	K0 IV	5318	0.26	6	Possible excess at IRS but not detected at MIPS-70

[a] Previously known/suspected excess source placed on FEPS program for purpose of gas detection experiment.

[b] The 70 um and some other data for this FEPS target derive from a GTO program; see § 2.

[c] See J. M. Carpenter et al. (2008a, in preparation) for caveats regarding *Spitzer* 70 μm photometry of this source.

[d] Candidate in this work.

REFERENCES FOR PREVIOUS DISCUSSION OF MID-INFRARED EXCESS.—(1) Silverstone 2000; (2) Meyer et al. 2004; (3) this paper; (4) Kim et al. 2005; (5) Patten & Willson 1991; (6) Spangler et al. 2001; (7) Moro-Martin et al. 2007; (8) Metchev et al. 2004; (9) Williams et al. 2004; (10) Sylvester & Mannings 2000; (11) Habing et al. 2001; (12) Sylvester et al. 1996; (13) Gregorio-Hetem et al. 1992; (14) Mamajek et al. 2004; (15) Neuhäuser et al. 2000; (16) Decin et al. 2000; (17) Fajardo-Acosta 1999.

TABLE 2

Spitzer PHOTOMETRY IN mJy

Source	3.6 μm	4.5 μm	8.0 μm	13 μm[a]	24 μm	33 μm[a]	70 μm	160 μm
Tier 1 Debris Disks (Excess $S/N_{70\,\mu m} \geq 3$)								
HD 105	1022.7 ± 22.0	645.4 ± 14.8	230.7 ± 4.9	83.3 ± 5.1	28.3 ± 1.2	20.5 ± 1.6	141.2 ± 14.3	110.1 ± 16.7
HD 377[b]	1029.1 ± 22.1	648.6 ± 14.9	234.7 ± 5.0	81.6 ± 5.0	36.6 ± 1.5	37.8 ± 2.7	162.0 ± 16.9	187.5 ± 50.4
HD 6963	1211.3 ± 26.0	752.9 ± 17.3	271.5 ± 5.8	91.2 ± 5.6	32.5 ± 1.3	21.8 ± 2.0	44.0 ± 8.6	61.1 ± 29.1
HD 8907[b]	1918.2 ± 41.2	1223.7 ± 28.1	427.3 ± 9.1	154.1 ± 9.4	51.3 ± 2.1	41.8 ± 3.5	247.4 ± 19.7	243.8 ± 42.3
HD 22179	311.7 ± 6.7	196.2 ± 4.5	71.0 ± 1.5	26.7 ± 1.7	11.1 ± 0.5	10.8 ± 0.8	35.9 ± 10.6	...
HD 25457	6259.7 ± 134.4	3956.3 ± 90.8	1412.3 ± 30.1	513.4 ± 31.2	205.8 ± 8.4	173.5 ± 10.8	307.2 ± 23.4	229.4 ± 67.5
HD 31392	1431.9 ± 30.7	891.7 ± 20.5	321.8 ± 6.9	112.4 ± 6.8	36.9 ± 1.5	19.1 ± 2.2	81.6 ± 10.1	82.0 ± 14.4
HD 35850	3030.3 ± 65.0	1917.9 ± 44.0	690.7 ± 14.7	246.6 ± 15.0	83.5 ± 3.4	54.6 ± 4.2	40.3 ± 8.0	...
HD 37484	893.7 ± 19.2	568.1 ± 13.4	202.2 ± 4.4	77.8 ± 4.7	54.6 ± 2.2	76.2 ± 4.7	114.4 ± 11.2	29.3 ± 14.0
HD 38207	287.0 ± 6.2	181.3 ± 4.2	64.6 ± 1.4	24.16 ± 1.5	16.5 ± 0.7	35.2 ± 2.1	184.6 ± 13.8	84.8 ± 40.7
HD 38529	5893.1 ± 126.5	3634.0 ± 83.4	1340.0 ± 28.6	467.3 ± 28.4	149.6 ± 6.1	85.7 ± 5.4	75.3 ± 12.4	84.8 ± 176.3
HD 61005	753.5 ± 16.2	472.3 ± 10.8	169.2 ± 3.6	62.3 ± 3.8	41.5 ± 1.7	110.0 ± 6.7	628.7 ± 45.4	502.6 ± 160.1
HD 72905[c]	6226.5 ± 133.6	3915.2 ± 89.9	1411.5 ± 30.1	...	163.5 ± 6.7	...	44.5 ± 6.3	...
HD 85301	1050.8 ± 22.6	652.1 ± 15.0	234.2 ± 5.3	86.6 ± 5.3	36.8 ± 1.5	28.5 ± 2.2	38.5 ± 7.5	−2.6 ± 15.8
HD 104860	724.8 ± 15.6	455.3 ± 10.5	162.5 ± 3.5	57.3 ± 3.5	19.9 ± 0.8	17.8 ± 1.8	183.1 ± 14.8	202.7 ± 27.0
HD 107146	1711.3 ± 36.7	1074.8 ± 24.7	384.4 ± 8.2	138.9 ± 8.5	59.8 ± 2.5	86.7 ± 5.7	669.1 ± 47.8	...
HD 122652	1260.6 ± 27.1	795.3 ± 18.3	283.1 ± 6.0	96.1 ± 5.8	35.2 ± 1.4	26.7 ± 3.5	83.1 ± 10.8	35.3 ± 27.3
HD 145229	1128.8 ± 24.2	717.4 ± 16.5	254.0 ± 5.4	91.7 ± 5.6	31.0 ± 1.3	22.1 ± 1.9	64.4 ± 8.6	33.9 ± 24.7
HD 150706	1715.1 ± 36.8	1077.0 ± 24.7	388.1 ± 8.3	135.7 ± 8.3	44.9 ± 1.8	28.0 ± 2.7	41.3 ± 8.5	−28.7 ± 19.9
HD 187897	1495.5 ± 32.1	934.1 ± 21.4	338.7 ± 7.2	113.5 ± 6.9	39.8 ± 1.6	23.2 ± 3.2	61.6 ± 9.3	−40.2 ± 65.3
HD 191089[b,c]	1071.7 ± 23.0	678.4 ± 15.6	242.2 ± 5.2	...	185.6 ± 7.6	...	544.3 ± 40.1	204.6 ± 44.6
HD 201219	816.4 ± 17.5	508.5 ± 11.7	181.3 ± 3.9	62.3 ± 3.8	22.0 ± 0.9	15.0 ± 1.6	42.4 ± 7.8	89.9 ± 42.2
HD 202917	519.2 ± 11.1	320.8 ± 7.4	117.3 ± 2.8	43.0 ± 2.6	19.2 ± 0.8	21.1 ± 1.5	37.1 ± 6.5	...
HD 209253	2008.4 ± 43.1	1285.3 ± 29.5	454.5 ± 9.7	167.6 ± 10.2	55.9 ± 2.3	48.1 ± 3.8	75.0 ± 10.6	17.6 ± 21.4
HD 219498	313.2 ± 6.7	196.1 ± 4.5	70.5 ± 1.5	25.5 ± 1.8	10.5 ± 0.4	9.5 ± 0.8	22.8 ± 4.0	−16.7 ± 50.7
Tier 2 Debris Disks (Excess $S/N_{70\,\mu m} \geq 2$ and <3)								
HD 17925[c]	7280.6 ± 156.3	4520.6 ± 103.8	1644.6 ± 35.1	624.0 ± 38.0	193.6 ± 7.9	134.7 ± 8.2	57.0 ± 12.3	...
HD 70573	381.6 ± 8.2	239.7 ± 5.5	86.4 ± 1.8	32.7 ± 2.1	10.4 ± 0.4	5.8 ± 0.8	14.8 ± 5.8	29.7 ± 30.0
HD 141943	849.1 ± 18.2	541.0 ± 12.4	193.1 ± 4.2	68.4 ± 4.2	27.3 ± 1.1	27.9 ± 2.0	37.6 ± 15.3	...
HD 204277	1847.5 ± 39.7	1172.2 ± 26.9	415.8 ± 8.9	143.8 ± 8.8	48.9 ± 2.0	27.3 ± 3.1	29.6 ± 10.8	...
HD 206374	1389.1 ± 29.8	871.1 ± 20.0	312.1 ± 6.7	106.5 ± 6.5	35.2 ± 1.4	54.1 ± 67.4	18.1 ± 6.8	−1.3 ± 30.8
MML 17	228.1 ± 4.9	145.0 ± 3.3	52.2 ± 1.1	19.2 ± 1.2	9.8 ± 0.4	9.5 ± 0.8	18.0 ± 7.7	−11.7 ± 85.7
Primordial Disks								
HD 143006	1069.4 ± 23.0	929.9 ± 21.4	792.1 ± 16.9	737.7 ± 44.9	2130.0 ± 136.0	4111.6 ± 250.1	3795.1 ± 267.7	3228.1 ± 400.2
PDS 66[b]	656.8 ± 14.1	521.4 ± 12.0	470.6 ± 10.0	720.9 ± 43.9	1874.0 ± 120.0	1779.2 ± 108.2	1672.0 ± 118.0	2138.4 ± 290.4
[PZ99] J161411.0−230536[b]	498.3 ± 10.7	401.9 ± 9.2	363.5 ± 7.8	349.1 ± 21.2	304.0 ± 12.5	209.3 ± 12.7	91.1 ± 13.3	43.1 ± 100.4
RX J1111.7−7620[b]	447.9 ± 9.6	363.5 ± 8.3	198.7 ± 4.4	160.9 ± 9.8	229.6 ± 9.4	217.5 ± 13.2	224.3 ± 17.8	445.4 ± 183.6
RX J1842.9−3532[b]	269.5 ± 5.8	216.2 ± 5.0	157.3 ± 3.4	100.7 ± 6.1	358.9 ± 14.7	429.4 ± 26.1	942.6 ± 67.4	844.0 ± 114.8
RX J1852.3−3700[b]	88.6 ± 1.9	58.5 ± 2.3	33.6 ± 1.2	35.0 ± 2.1	472.2 ± 19.4	749.4 ± 45.6	1367.0 ± 96.8	1490.1 ± 195.7

NOTES.—Uncertainties include both internal and calibration terms. See § 2 for details.

[a] The 13 and 33 μm synthetic photometry is derived from IRS low-resolution spectra. For HD 206374 the 33 μm spectrum has significant noise features appearing within the synthetic passband, resulting in low S/N.

[b] The 160 μm photometry is from a GO-2 or GO-3 program following up the 70 μm detections reported here. Integration times are longer than standard FEPS observing procedures; see § 2.

[c] The 13 and 33 μm synthetic photometry is derived from IRS high-resolution rather than low-resolution spectra.

see also Kim et al. (2005) for 160 μm procedures. The photometric uncertainties are also discussed in J. M. Carpenter et al. (2008b, in preparation). They were assessed for the IRAC and MIPS 24 μm data by computing the error in the mean of the flux densities derived from individual frames, with an adopted floor. These (presumed) photometric uncertainties are then validated by examination of flux density histograms and of source colors. For MIPS 70 μm data, the photometry was performed not on individual images as for data at all other wavelengths, but on the final stacked/mosaicked image only, with the error calculated by propagating the measured rms deviation in the sky area over the source aperture. Thus, the only validation of the internal uncertainty comes from the Kurucz model comparison (illustrated below). The random errors in the photometry at 70 and 160 μm were estimated from the square root of the variance observed in the sky annuli of the final resampled mosaics for these background-limited observations. After careful analysis we find that the MIPS 70 μm internal uncertainties must be inflated by a factor of 1.5 to account for the scatter in the quantity (data minus model), as discussed in detail in J. M. Carpenter et al. (2008a, in preparation). Calibration uncertainties were taken from the *Spitzer* Observers' Manual version 7.0 (<2% for the IRAC bands, 4% for MIPS 24 μm, and 7% for MIPS 70 μm) and dominate the error in our absolute photometry for sources with $S/N \gg 1/\sigma_{calib}$ (see Table 2 for relevant details). We make use of internal and internal+calibration uncertainties at separate points in our analysis. For comparison between simple models and the data, we also use synthetic photometry points constructed from the IRS spectrophotometric data (S14 processing) with square bandpasses of 12%–15% width centered at 13 and 33 μm (flux-weighted average wavelengths 13.17 and 32.36 μm, assuming a Rayleigh-Jeans SED).

3. IDENTIFYING 70 μm DETECTIONS AND EXCESS SOURCES

In this section we first establish the reliability of the 70 μm source detections and their association with the intended FEPS target. We consider sensitivity, cirrus, and confusion as limitations. The possible detections at 70 μm are defined by (1) photometric measurements with $S/N > 2$ at 70 μm using internal errors, (2) visibility to the human eye and point-source morphology on the 70 μm images, and (3) positional alignment with the corresponding 24 μm point sources. From the detections at 70 μm, we then define via color-color diagrams and excess S/N histograms the subsample with $S/N > 2$ excesses at 70 μm, using both internal and calibration errors. Finally in this section, we present SEDs for these sources. Table 1 contains our 70 μm excess candidates and includes notes on several sources for which the determination of excess detection in 70 μm is not straightforward.

3.1. *Sensitivity Considerations*

FEPS achieves *photospheric sensitivity* with $S/N > 30$ for 100% of the program objects at all *Spitzer* broadband wavelengths $\leq$24 μm, and with $S/N > 3$ for 90% of the program objects in IRS spectrophotometry out to 35 μm. At 70 μm, however, detecting photospheres of solar-type stars at distances greater than about 12 pc is not feasible in the launched version of *Spitzer* in less than several hours of integration. As our targets range from tens to hundreds of parsecs, a very small fraction of our sample was proximate enough for detection at 70 μm in the absence of excess emission. A few such photospheres are indeed detected: HD 13974 (11 pc) and HD 216803 (7.6 pc), the latter observed as part of GTO time (Rieke), and also potentially HD 17925 (10 pc), which is noted below as only a low significance excess object.

Our integration times (§ 2) were chosen to be sensitive to a minimum dust level relative to that inferred for dust in our own solar system (e.g., Landgraf et al. 2002) as it appeared earlier in its evolutionary history. Such evolution has been described as having a power-law behavior in certain regimes: roughly τ^0 until collisional equilibrium is reached, transitioning to τ^{-1} by several hundred million years, then to τ^{-2} beyond a few billion years (e.g., Dominik & Decin 2003; Wyatt 2005). These canonical regimes are well sampled by the FEPS age distribution. A realistic model has more structure than the simple power-law estimates above, which are just guides to the behavior. The simulations that we used (D. Backman 1999, private communication; see also Meyer et al. 2007) assume an initial planetesimal belt of 30 $M_\oplus$ distributed between 30 and 50 AU that undergoes collisional evolution; material is subsequently parsed according to a Dohnanyi (1969) fragment mass distribution down to small sizes. For a fiducial source at distance 30 pc and luminosity 1 $L_\odot$, the dust evolution predicts a change in 70 μm flux density from 180 to 50 mJy for source ages between 150 and 1500 Myr. Given the actual age and distance/luminosity distribution of our sample, approximately $\frac{1}{3}$ of our targets are younger than 150 Myr and almost all FEPS targets 150–1500 Myr have 3 σ sensitivity at 70 μm exceeding this dust model. Our survey is sensitive to dust emission 5 times greater than that estimated from the projected young solar system model for most of the remaining $\sim\frac{2}{3}$ of the targets, and sensitive to 10 times greater emission for all but a few (with the limitations primarily driven by the increased distance range required to find young targets). For older (nearby) stars, our survey was sensitive to dust emission roughly 5–20 times the current solar system level (or 9–36 mJy in the excess, for the fiducial source above).

Figure 1 shows, for the full sample of stars observed under the auspices of FEPS, the distribution of S/N at 70 μm and the distribution of measured 70 μm flux density, separately for detections and nondetections. There is significant overlap among the detected and nondetected flux densities due to source-to-source variation in astrophysical background, the main sensitivity limitation. The typical <2 σ nondetection has measured flux density of about 5–10 mJy (median noise = 9 mJy), while the typical >2 σ detection has measured flux density of >30 mJy (median = 60 mJy and mean = 80 mJy). The 2 σ level is used rather than a more stringent 3 or 5 σ threshold in order to identify all reasonable candidate 70 μm sources, including those that require confirmation.

Assuming that our (estimated) uncertainties are accurate, for our sample of 328 sources we expect <1 to fall above +3 σ and $\sim$8 to fall above +2 σ if the data follow a Gaussian distribution. Therefore, $\sim$7 should fall between 2 and 3 σ. We observe 33 sources above 3 σ and 11 sources between 2 and 3 σ. Accordingly, possibly one of the >3 σ detections and probably most of the 2–3 σ detections are noise and should be treated with caution. Only a portion of the latter survive our other cuts for source detection (image visibility and positional alignment) and are subsequently identified as objects with excess emission. They are noted in Table 1 as those also having *excess* S/N between 2 and 3 σ (except for HD 17925, which is a 4.6 σ detection in observed flux density but only a 2.9 σ significant excess).

Approximately 10% of FEPS targets are detected at 70 μm, and the remainder are undetected, having flux density upper limits.[9] In Figure 2 we illustrate the measured flux densities and 1 σ noise values, versus source distance and stellar age. No trends

[9] We note that some of the sources represented here as upper limits at 70 μm have been identified as having dust excesses from IRS data and subsequently were detected at 70 μm in deeper follow-up observations conducted by the FEPS team through GO programs (see J. S. Kim et al. 2008, in preparation).

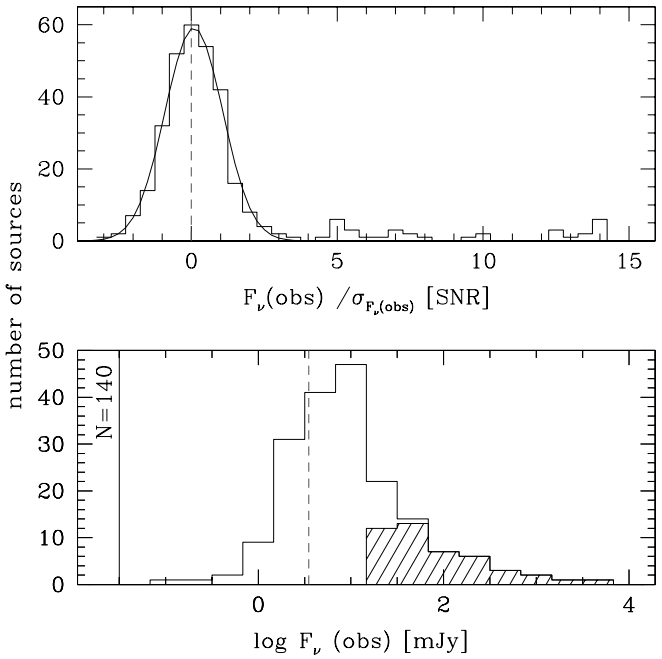

FIG. 1.—Histograms of 70 μm S/N and measured flux density. *Top*: Measured flux density divided by uncertainty. A Gaussian fit at $|S/N| < 3$ has a mean of 0.09 and a dispersion of 0.99 and is shown as the solid curve; the vertical dashed line indicates zero, for reference. Based on this distribution, which validates the arbitrarily inflated (by a factor of 1.5) noise estimates, secure 70 μm detections are those sources with $S/N > 3$, where each S/N bin contains less than one spurious noise source. *Bottom*: Logarithm of the 70 μm flux densities for candidate detections having flux density larger than twice the error (*hatched histogram*) compared to the measured 70 μm flux densities for all sources (*open histogram*). The unclosed bin to the left represents objects with formally negative flux densities (left side of the Gaussian in top panel). For comparison, the typical 3 σ detection limits from *IRAS* and *ISO* at 60 μm were 500 and 100 mJy, respectively. The vertical dashed line indicates the estimated "5 σ" confusion limit of 3.2 mJy based on the MIPS 70 um source density criterion for confusion (Dole et al. 2003, 2004b). When the nondetections (*open histogram*) are plotted as 1 σ rather than measured values, the histogram indeed piles up at this limit (see, e.g., lower bounds in Fig. 2). [*See the electronic edition of the Journal for a color version of this figure.*]

are apparent in the relative distribution of the upper limits with these variables. This is consistent with the interpretation that our sensitivity at 70 μm is dominated by infrared background and cirrus effects, as expected. A K-S test comparing the distributions of photometric background for the detected and nondetected sources indicates that they might not be consistent with having been drawn from the same parent population [$P(d)$ less than a few percent]. However, the distance and age distributions of detected and nondetected sources are both consistent with having been drawn from the same parent based on the K-S test [$P(d)$ greater than a few percent], the distances being potentially more distinguishable than the ages. The only obvious trend in Figure 2 is that younger sources (which typically are more distant than the older sources in our sample) tend to have a larger upper range to their 70 μm flux densities (indicating higher values of $L_{\rm dust}/L_*$). We return to this point in § 6.1.

3.2. *Cirrus and Confusion Considerations*

We take care to ensure not only the detection of signal above the noise at 70 μm but also that the signal is from the intended FEPS target. Peaks in the Galactic cirrus structure or confusion with extragalactic contaminants are considerations at 70 μm.

Each candidate 70 μm source was thus inspected by eye to check for pointlike appearance. No obvious examples of resolved extended emission, which could indicate contamination from cirrus, were identified. Such emission can also be identified via relative photometry in larger versus smaller apertures. As reported in J. M. Carpenter et al. (2008b, in preparation), two sources are identified with larger than expected flux ratios in photometry derived from bigger versus smaller apertures. Both are confused by nearby 70 μm–bright objects that were removed by PSF fitting before the final photometry of the FEPS target was measured and reported. Based on this analysis, cirrus contamination is an unlikely explanation for the 70 μm point-source detections reported here.

The MIPS 70 μm FWHM is 16″ (9.8″ pixels) compared to 5.4″ FWHM (2.5″ pixels) at 24 μm. Because of the dependence of diffraction on wavelength, a 70 μm source near the center of the MIPS field may not be spatially coincident with the targeted source that is detected with a higher accuracy centroid and at higher S/N at shorter wavelengths. Unassociated contaminants such as active galactic nuclei and ultraluminous infrared galaxies have 70 μm/24 μm flux density ratios of 0.5–3 (e.g., Frayer et al. 2006), similar to those observed for our sources (e.g., Fig. 4 below), which we interpret as due to circumstellar dust disks. Thus, comparing the centroids of detections at 24 and 70 μm is particularly important. The absolute pointing of *Spitzer*'s focal plane array pixel centers is assessed by the Pointing Control System, which is astrometrically tied to the Two Micron All Sky Survey (2MASS). The 1 σ uncertainties on the absolute pointing reconstruction are better than 1.4″ at 24 μm ($\sim\frac{1}{4}$ beam) and 1.7″ at 70 μm ($\sim$1/10 beam). Therefore, 24 μm coordinates should be within 1.4″ of corresponding 2MASS sources, and the difference between 24 and 70 μm positions should be $<2.2'' = (1.4^2 + 1.7^2)^{1/2}$ in the high-S/N limit. Measured positional offsets thus provide a good, although not robust, discriminant between associated and unassociated sources. We use the 24 and 70 μm images for this comparison in order to keep the relative investigation to within the *Spitzer* focal plane and free of absolute positional calibration.

Figure 3 shows the right ascension and declination offsets between the 24 and 70 μm point-source positions. At 24 μm, pixel positions were determined from Gaussian centroiding and the corresponding right ascension and declination derived from the distortion-corrected image headers. At 70 μm, Gaussian centroiding was applied to a 44″ squared region centered at the expected source position. In Figure 3 two sources (HD 141943 and HD 70573) are rather large outliers, $>\frac{1}{2}$ of the 70 μm beam size, while two others (HD 206374 and HD 201219) are offset by $\sim\frac{1}{4}$ beam. The empirical 1 σ scatter in Figure 3 is 2.47″, roughly 10% higher than the minimum 2.2″ from above. We implement a cutoff of 2.75″ (<2 σ) to consider a 70 μm detection as being coincident with the source seen at 24 μm. We retain HD 201219, however, as its known companion, which has been subtracted for photometry purposes, still influences the 70 μm image centroid. We also retain HD 206374, which is in the low-S/N regime, and thus a large offset is possible.

We also consider the probability of false association of the 70 μm point source with the FEPS target even when there is apparent spatial coincidence with a 24 μm point source that can be robustly associated itself with the intended target, both positionally and, in many cases, by having the expected photospheric flux density. We estimate the probability of a chance superposition with a background galaxy that dominates the flux at 70 μm, adopting the methodology of Downes et al. (1986). For a surface density of objects $\Sigma(F > B)$ having flux densities, F, brighter than B, the probability of finding one of these galaxies within radius r of the FEPS target is given by the Poisson distribution

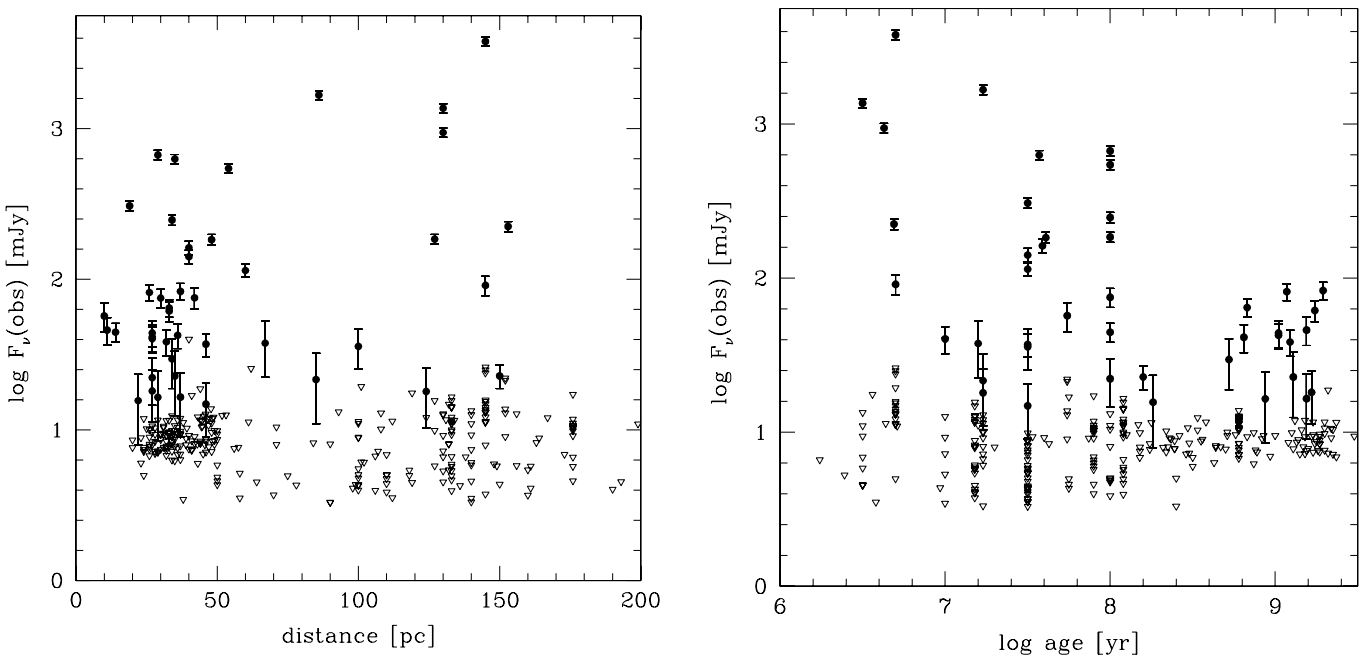

FIG. 2.—Sensitivity of the FEPS 70 μm data as a function of source distance and age. Filled symbols with error bars represent candidate detections (flux density larger than twice the error), while open triangles represent upper limits (plotted now at their 1 σ values rather than the "measured" values illustrated in Fig. 1). Although there is wider scatter in the upper limits for distances >50 pc and ages <300 Myr with approximately $\frac{1}{2}$ of such cases having more sensitive limits than closer and older stars, any systematic trends with distance or age in the relative distribution among the upper limits are weak. This is consistent with the interpretation that 70 μm sensitivity is dominated by infrared background and cirrus as intended with our integration time strategy.

$P = 1 - e^{-\Sigma(F>B)\pi r^2}$. From Dole et al. (2004a), we expect $\Sigma < 1.1 \times 10^{-1}$, $<1.1 \times 10^{-2}$, and $<3 \times 10^{-3}$ galaxies arcmin^{-2} at 70 μm flux density levels of >10, >50, and >100 mJy, respectively, or <2.1, <0.2, and <0.06 galaxies per MIPS 70 μm mosaic ($\sim$20 arcmin^2 after combining several individual $2.6' \times 5.25'$ raster images). Considering the FEPS data set as a whole, approximately $\frac{1}{3}$ of all (324 visually examined) FEPS 70 μm mosaicked images have an obvious source somewhere in the field, with $>\frac{1}{3}$ of these $\frac{1}{3}$ (or 40 sources) within $\frac{1}{2}$ beam width of the image center, the expected position of the FEPS target. Among the near-coincident sources we observe 0, 18, and 26 sources at flux density levels <10, <50, and <100 mJy, respectively, with 14 sources >100 mJy (including those with the relatively large offsets noted above). Thus, the probability of a chance superposition of a galaxy within our search radius of 2.75″ emitting $F_{70\,\mu m} \geq 10$, 50, and 100 mJy is $P = 7.26 \times 10^{-4}$, 7.25×10^{-5}, and 1.98×10^{-5} per object, respectively. This corresponds to a probability of <24%, <2%, and <1% that one target is contaminated at the >10, >50, and >100 mJy levels, respectively, for the whole sample of 328.

At 24 μm, the faintest detection among our 328 FEPS targets is $F_{24\,\mu m} \sim 1$ mJy. The 24 μm surface density due to extragalactic objects at 1 mJy is $\Sigma \sim 0.15$ arcmin^{-2} (Papovich et al. 2004), implying a maximum probability per star of $P = 9.9 \times 10^{-4}$ for a faint galaxy within 2.75″ contributing to the measured 24 μm flux density (using the radius appropriate to the agreement between the 24 and 70 μm positions; Fig. 3). Despite having a higher potential than at 70 μm for extragalactic contamination, our 24 μm sources in most cases have flux densities consistent with expected photospheric emission; this argues that they indeed emanate from the intended FEPS target. For those with measured excesses at the mJy level, there is a <33% chance that one source suffers extragalactic contamination among the sample as a whole.

We conclude that the 70 μm emission, distributed in flux as we have shown in Figure 1, and emanating from the same source as the 24 μm emission as we have shown in Figure 3, is likely associated directly with the targeted FEPS stars.

3.3. *Color-Color Diagrams*

Color-color diagrams are an efficacious way to identify objects with unusually red colors due to circumstellar dust. In Figure 4 we show several different flux ratios involving the 70 μm band observed with *Spitzer*. As mentioned above, the FEPS 70 μm data are dominated by upper limits. For clarity, we therefore indicate separately the maxima and the measured colors involving 70 μm photometry. Although we cannot use exclusively these color-color diagrams to identify 70 μm excess sources, we can employ them in a rudimentary assessment of the hot, warm, and cold dust components in the circumstellar environments of FEPS sources.

The top panels of Figure 4 show 4.5 μm/3.6 μm and 70 μm/3.6 μm flux density ratios; the abscissa is approximately photospheric for the great majority of FEPS stars, while the ordinate is sensitive to cool dust. The few red outliers in the 4.5 μm/3.6 μm flux density ratio are also among the reddest objects in the 70 μm/3.6 μm flux density ratio, as expected if they have both hot inner and cool outer dust. These sources exhibit evidence for primordial (gas-rich) disks. In contrast to the narrow 4.5 μm/3.6 μm flux density ratio, there is a large range in the 70 μm/3.6 μm flux density ratio for those stars detected at 70 μm (*top right panel*), but an equally large range in the distribution of color limits (*top left panel*). Notable is the admixture along the ordinate of the detections and upper limits. Even accounting for the fact that the limits are plotted at 1 σ levels (consistent with Fig. 2) while the detections are all >2–3 σ, the most stringent upper limits in the top left panel appear a factor of several lower compared to the detections reported in the top right panel. Such variation along the ordinate among the detected sources likely reflects real differences in debris disk properties. Recall, however, as argued above based on K-S statistics, that variation in source background may play a

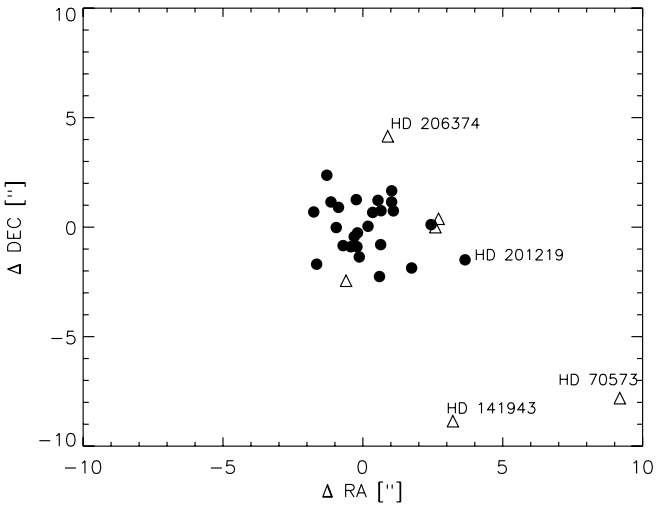

FIG. 3.—Positional offsets between the centroids of 24 and 70 μm point sources. Centroiding errors depend on S/N, which has a large range for our sample as illustrated for the 70 μm data in Fig. 1. Filled symbols indicate sources with 70 μm detection S/N > 4, while open triangles are lower S/N detections. The empirical scatter (1 σ) in the position differences is 2.10″ in right ascension, 2.53″ in declination, and 2.47″ in total separation.

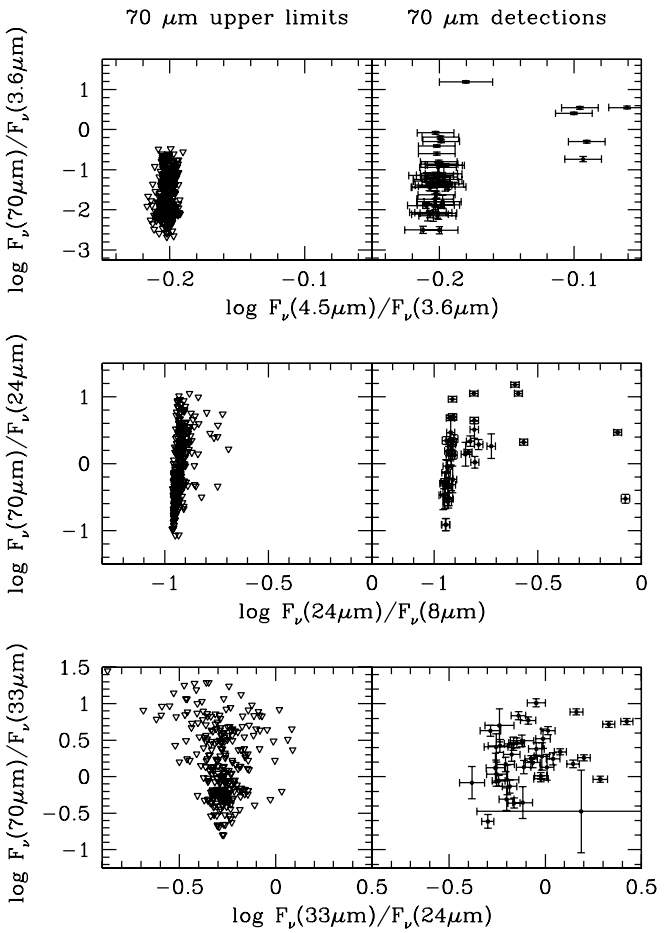

FIG. 4.—Color-color diagrams highlighting 70 μm photometry. Sources detected at S/N(70 μm) > 2 are distinguished in the right panels from the nondetections in the left panels; the latter are plotted as 1 σ upper limits to illustrate the admixture in color among sources in the FEPS sample between 70 μm signal and 70 μm noise. Note the horizontal broadening of the data distribution in the 24–33 μm color (*bottom*) panels relative to the top panels. The source with large error bar in the bottom right panel is due to a particularly noisy long-wavelength IRS spectrum; see Table 2.

significant role in 70 μm detection despite our attempts to observe the lowest background sources of given age and distance.

The middle and bottom panels of Figure 4 illustrate 70 μm/24 μm versus 24 μm/8 μm and 70 μm/33 μm versus 33 μm/24 μm flux density ratios, respectively. Again, by comparing the left and right panels it can been seen that 70 μm detections are interspersed in color with 70 μm upper limits. Further, a subset of the stars is redder in the 24 μm/8 μm and/or 33 μm/24 μm flux density ratios compared to the bulk of the sample. These are "warm" excess sources. Some but not all such objects are also detected at 70 μm, which enables better constraints on the bulk dust characteristics than in cases in which the excess is detected in only a single band.

Our focus in this paper is on the subset of objects with excesses detected at 70 μm. Typically these sources are blue along the abscissae of Figure 4, implying that they are close to photospheric at wavelengths shorter than 24–33 μm. Several of the brightest debris disks in our sample (specifically HD 61005, HD 107146, HD 38207, HD 191089, and HD 104860) can be distinguished in the color-color plots; however, additional analysis is needed to identify most debris disk candidates.

3.4. *Excess Signal-to-Noise Ratio Histograms*

The majority of sources detected at 70 μm are dominated by the circumstellar contribution to the flux density. However, the photospheric contribution at 70 μm is not negligible for all sources and must be modeled accurately in order to characterize the excess. We employ a Kurucz model of the underlying stellar photosphere in order to more robustly identify individual objects with 70 μm excess than is possible from color-color diagrams and to analyze the S/N in the excess.

As described in more detail by J. M. Carpenter et al. (2008b, in preparation), available *BV* (Johnson, Tycho), *vby* (Stromgren), H_p (*Hipparcos*), *RI* (Cousins), and JHK_s (2MASS) photometry data were used in combination with initial estimates of temperature, surface gravity, and metallicity based on spectroscopic data from the literature, to find a best-fit Kurucz model. Kurucz model flux densities were converted to magnitudes in each of the available optical/near-infrared filters via multiplication with the combined filter, atmospheric transmission, and detector response curves as in Cohen et al. (2003a, 2003b and references therein). In general, surface gravity and metallicity were fixed at $\log g = 4.5$ cm s^{-2} and [Fe/H] = 0.0, and the effective temperature and normalization constant were the fitted parameters. The line-of-sight extinction was fixed to $A_V = 0.0$ for stars within 75 pc; beyond this distance A_V was initially estimated from the literature but then varied as a free parameter in the fits for all stars not in clusters or with estimated ages younger than 30 Myr (which may suffer some obscuration). The best fit was defined in a least-squared sense. The formal uncertainty in the resulting photospheric projection to the *Spitzer* bands is typically 2%–3%.

With a model of the expected photospheric flux, the excess above the photosphere is computed as the difference between the observed and Kurucz in-band flux densities. The S/N in the excess is defined as this difference divided by the root-sum-squared error in the observed flux densities and the photospheric projection. Figure 5 shows histograms of the resulting S/N *in the excess* at 70 μm. The excess S/N distribution for the nondetections and indeed for the full FEPS sample is peaked near zero, suggesting the expected dominance by photometric noise at this wavelength. The median, mean, and dispersion of the distribution are −0.25, −0.22, and 0.84, respectively, in units of S/N. The

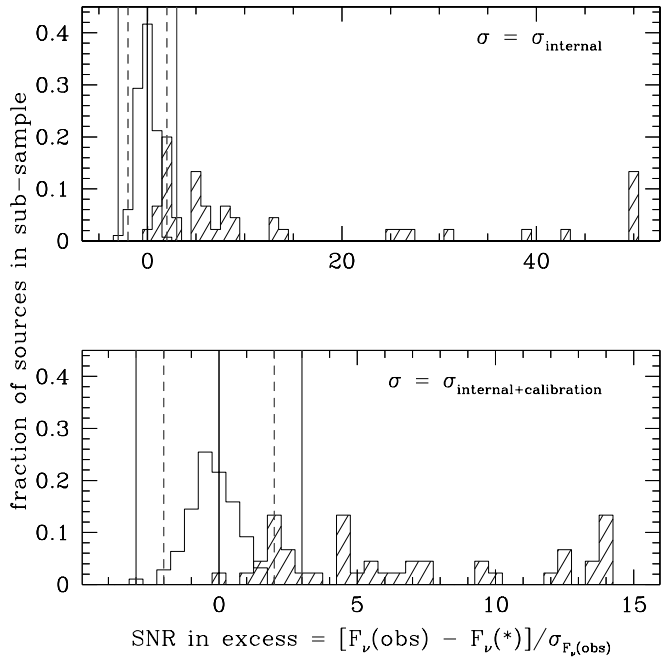

FIG. 5.—S/N in the 70 μm excess following subtraction of a photospheric model from the observed photometry. The top panel considers only internal errors in computing excess S/N, while the bottom panel considers both internal (random) and calibration (systematic) errors. Vertical lines indicate excess S/N = 0 (*black*) and $\pm$2, 3 (*gray*). Note that plots are fractional for each of the two subsamples, which separately add across the bins to unity. The open histogram represents sources not detected at greater than 2 σ at 70 μm. The excess S/N of this sample is centered near zero excess (although formally negative, with mean/median about -0.2, perhaps suggesting that we have overestimated the contribution from the stellar photosphere) and has a roughly Gaussian distribution as expected from pure noise; no sources have excess S/N < -3, and seven have excess S/N between -3 and -2. The hatched histogram includes only those FEPS objects convincingly detected at 70 μm, as detailed in the text, and is biased toward significant positive excess. HD 13974 is the only statistically significant photospheric detection at 70 μm among FEPS objects (flux density S/N = 5 and excess S/N = 0.88 and 0.82 from top and bottom panels, respectively). HD 216803, observed as part of a GTO program, is also a detected photosphere at flux density S/N = 5 and excess S/N = -0.16 and -0.15 in the top and bottom panels, respectively. Thirty-one FEPS sources have excess S/N > 3, and six have excess S/N between 2 and 3. [*See the electronic edition of the Journal for a color version of this figure*.]

>2 σ 70 μm excess sources have median, mean, and dispersion of 6, 15, and 17, respectively, in units of S/N. Using only the internal uncertainty, the significance of the detected excesses can be as high as S/N = 50, while using the total uncertainty (root sum square of common calibration and individual internal uncertainty terms), no source has excess S/N > 10.

We have defined a sample of 70 μm excess sources as follows. The excess S/N distribution of Figure 5 is centered near (but not exactly at) zero with dispersion that is close to (but not exactly) the value of unity that would be expected from Gaussian noise (including the imposition of an additional 50% scale factor in the 70 μm flux density uncertainties as discussed in § 2). We therefore consider most robust those sources that have >3 σ (formally 99.6% confidence) excesses at 70 μm when they are apparent from *both* the internal-only and total uncertainty assessments. These are our "tier 1" sources. Our "tier 2" sources are those with 2–3 σ excesses at 70 μm. That the mean in Figure 5 is significantly (with respect to the error in the mean) negative suggests a systematic offset with respect to the Kurucz models, in the sense that we are somehow overcorrecting for the photosphere. This may indicate that some of the 2–3 σ excess sources we have designated in Table 1 are in fact slightly more significant, by 0.22 σ, than our estimates.

Note in Figure 5 that no sources have excess S/N < -3 and seven have excess S/N between -3 and -2, while 31 sources have excess S/N $> +3$ and six have excess S/N between +2 and +3.[10] The number of 2–3 σ significant excess sources is seemingly consistent with random noise, both empirically and from Gaussian statistics. We note these sources with caution and distinguish them clearly as tier 2 objects in the remainder of this paper.

3.5. *Summary and Spectral Energy Distributions*

In summary, we find 31 primordial and debris disk targets with excess $S/N_{70\,\mu m} > 3$. Excess $S/N_{70\,\mu m}$ between 2 and 3 is measured for an additional six candidate debris excess objects. These sources meet, in addition to the flux density criteria, the pointlike appearance and positional coincidence requirements stated earlier. In Table 1 we present the 70 μm excess sources selected as described above, along with the stellar parameters (distance, spectral type, luminosity, and age as adopted by FEPS). In Table 2 we present corresponding *Spitzer* photometry (measured flux densities, uncertainties), and in Table 3 we present the calculated excesses and significances above the adopted model stellar photospheres at 13, 24, 33, 70, and 160 μm. Of the sources selected to have 70 μm excess attributed to debris dust, more than half, less than half, and a single source also have significantly measured excesses at >33, 24, and 13 μm, respectively; none of the debris disk candidates have excess detected at 8 μm.[11] The excess amplitudes at 70 μm range from 1.6 to over 300 times the photosphere (median is 20 times photosphere), while at 33 μm the median excess amplitude is equal to (100% of) the photosphere, at 24 μm it is 40% of the photosphere, and at 13 μm it is 17% of the photosphere.

Several sources deserve specific comment. First, some objects selected for the FEPS probe of disk gas evolution based on claimed *IRAS*- or *ISO*-based 60 and/or 90 μm excesses are not confirmed from this analysis with *Spitzer*. These include ScoPMS 214,[12] HD 41700, HD 216803, and HD 134319, which were discussed in Pascucci et al. (2006). We include these four objects in Table 1 for completeness, but they do not appear in subsequent tables or figures. Second, there are additional sources selected for the gas experiment for which FEPS is not obtaining 70 μm observations because the objects are part of GTO programs with MIPS (HD 216803, HD 202917, HD 17925, and HD 72905). These objects exhibit excess emission based on *Spitzer* data and are included in Table 1 and our subsequent analysis.

In Figures 6 and 7 we present SEDs for the FEPS 70 μm excess sources. Included are ground-based data from Tycho and 2MASS along with newly presented *Spitzer* IRAC, IRS, and MIPS photometry and IRS spectrophotometry. Simple blackbody dust models as discussed in the next section (§ 4) are also overplotted.

There are six FEPS 70 μm excess sources shown in Figure 6 with large excesses that are broad in wavelength and associated with some of the youngest stars in our sample. These are likely primordial disks (see Silverstone et al. 2006; Bouwman et al. 2008). While the four strongest (in terms of monochromatic excess) of these six are in fact the largest 70 μm excess sources among the entire FEPS sample, two of the six ([PZ99] J161411.0−230536 and RX J1842.9−3532) are weaker at 70 μm and have inferred $L_{\rm disk}/L_*$ lower than several (much) older debris disks.

[10] We can compare these *excess detection* numbers (31 and 6) to the *source detection* numbers at these same significance levels (33 and 11, as reported in § 3.1).

[11] J. M. Carpenter et al. (2008a, in preparation) discuss additional sources within our 70 μm excess sample with low-amplitude excesses at wavelengths <35 μm that were not apparent from our analysis comparing to Kurucz models.

[12] J. M. Carpenter et al. (2008a, in preparation) find that this source has weak MIPS 24 μm and IRS excess.

TABLE 3
Fractional Excess Flux and Excess Signal-to-Noise Ratio

Source	13 μm		24 μm		33 μm		70 μm		160 μm	
	F_{excess}/F_*	F_{excess}/σ[a]	F_{excess}/F_*	F_{excess}/σ[a,b]	F_{excess}/F_*	F_{excess}/σ[a,b]	F_{excess}/F_*	F_{excess}/σ[a]	F_{excess}/F_*	F_{excess}/σ[a]
Tier 1 Debris Disks (Excess S/N$_{70\,\mu m} \geq 3$)										
HD 105	0.06	0.8	0.13	2.4	0.55	4.5	49.34	9.7	194.6	6.6
HD 377	0.00	0.0	0.41	6.5	1.75	8.8	54.77	9.4	320.6	3.7
HD 6963	−0.06	−0.9	0.05	0.9	0.33	2.6	11.73	4.7	87.00	2.1
HD 8907	0.01	0.1	0.05	0.9	0.63	4.5	44.57	12.3	222.4	5.7
HD 22179	0.09	1.2	0.42	6.1	1.62	7.9	40.12	3.3	...	...
HD 25457	0.04	0.6	0.31	4.6	1.10	8.0	16.54	12.4	64.18	3.3
HD 31392	−0.003	−0.1	0.02	0.4	0.01	0.1	19.27	7.7	100.3	5.6
HD 35850	0.07	1.1	0.14	2.6	0.41	3.7	3.94	4.0	...	...
HD 37484	0.10	1.3	1.43	13.6	5.43	13.5	44.67	10.0	57.2	2.1
HD 38207	0.08	1.0	1.31	13.0	8.36	14.7	231.5	13.4	532.1	2.1
HD 38529	−0.04	−0.5	−0.04	−0.6	0.04	0.5	3.33	4.7	23.29	0.5
HD 61005	0.07	1.0	1.24	12.6	10.24	14.9	302.6	13.8	1207	3.1
HD 72905	...	...	−0.16	−2.3	...	...	1.68	4.4	...	...
HD 85301	0.02	0.3	0.36	5.8	1.00	6.4	11.73	4.7	−5.21	−0.2
HD 104860	0.01	0.2	0.10	1.9	0.87	4.6	89.83	12.2	499.6	7.5
HD 107146	0.03	0.5	0.40	6.3	2.84	11.2	139.0	13.9	...	...
HD 122652	−0.05	−0.8	0.08	1.5	0.57	2.7	22.56	7.4	48.82	1.3
HD 145229	0.02	0.3	0.09	1.6	0.46	3.7	19.19	7.2	51.86	1.3
HD 150706	0.02	0.2	0.05	1.0	0.24	2.0	7.69	4.3	−31.01	−1.5
HD 187897	−0.06	−0.9	0.03	0.6	0.14	0.9	13.29	6.2	−47.42	−0.6
HD 191089	...	...	5.94	20.8	...	...	181.7	13.5	340.6	4.6
HD 201219	−0.03	−0.4	0.07	1.4	0.39	2.7	17.56	5.2	194.9	2.1
HD 202917	0.16	2.2	0.63	8.8	2.39	9.9	27.19	5.5	...	...
HD 209253	0.09	1.2	0.14	2.4	0.86	5.7	12.69	6.5	14.96	0.8
HD 219498	−0.005	−0.1	0.29	4.4	1.19	6.2	23.95	5.4	−91.78	−0.3
Tier 2 Debris Disks (Excess S/N$_{70\,\mu m} \geq 2$ and <3)										
HD 17925	0.07	1.0	−0.21	−4.2	0.37	4.2	1.74	2.9	...	...
HD 70573	0.10	1.2	0.09	1.8	0.15	0.9	12.95	2.4	138.3	1.0
HD 141943	0.08	1.1	0.35	5.6	1.61	8.6	15.66	2.3	...	...
HD 204277	−0.05	−0.7	0.02	0.3	0.08	0.6	4.53	2.3	...	...
HD 206374	−0.05	−0.8	−0.03	−0.7	1.86	0.5	3.61	2.1	−2.71	−0.1
MML 17	0.07	0.9	0.72	8.6	2.13	8.1	27.17	2.3	−92.5	−0.1

[a] Excess S/N is calculated using total uncertainty on the photometry.
[b] Some sources indicated here as having low S/N in the excess are reported as significant excesses by J. M. Carpenter et al. (2008a, in preparation) based on empirical colors rather than Kurucz model analysis. Specifically, that paper reports that for those stars in this table that were not selected for FEPS based on previous suspicion of mid-infrared excess (19 of the 31), only HD 187897 and HD 206374 lack 33 um excess and only HD 206374, HD 187897, HD 150706, HD 38529, and HD 31392 lack 24 um excess, with excess defined at the >3 σ level. Of the remaining 11 previously suspected mid-infrared excesses, the majority are confirmed at 33 μm from our own analysis (just HD 70573 is indeterminate).

There are 25 FEPS 70 μm excess sources shown in Figure 7 that are debris disk candidates having >3 σ significance in the 70 μm excess. A further six have >2 σ but <3 σ significance (see Table 1). The SEDs are photospheric over several octaves in wavelength with evidence of infrared excess only longward of 13 μm. Of these 31 total sources, 7 were presented in various earlier FEPS papers and 10 in literature previous to that; thus, 14 debris disks are newly announced here from FEPS. For this ensemble, detections and upper limits at submillimeter and millimeter wavelengths, where available from other investigations of FEPS targets (e.g., Williams et al. 2004; Carpenter et al. 2005; Najita & Williams 2005), are included in Figure 8, which plots the energy distributions in units where the long-wavelength Rayleigh-Jeans tail of the Planck function is flat.

4. DEBRIS DISK MODELING

Having selected a sample of objects likely to be surrounded by cool dusty material, we proceed in this section to model the plausible radial distribution of the dust around these stars using basic assumptions. We take the simplest possible approach to modeling the data and add complexity only as warranted. We consider the scenario in which a dust grain of given size and composition is in thermal equilibrium with the stellar radiation field. We assume emission from optically thin ensembles of grains, which we justify post facto by the resulting low fractional excess luminosities ($L_{dust}/L_* < 10^{-3}$).

First, we consider single-temperature blackbody fits, which have the minimum number of free parameters, to the observed excess emission (§ 4.1), and then we explore multitemperature models for selected sources (§ 4.2). In § 4.3 we summarize results from more detailed modeling pursued elsewhere within the FEPS program using sophisticated radiative transfer dust models with many free parameters, including grain size distributions. In § 4.4 we discuss upper limits on the amount of dust potentially located interior to our inferred inner disk annuli.

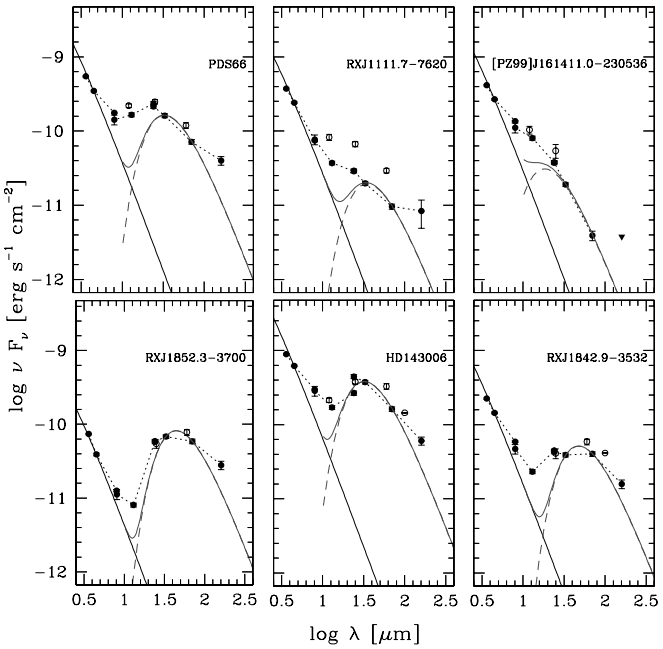

FIG. 6.—SEDs for the 70 μm excess sources in the FEPS "primordial" disk sample. We use the "average weighted" wavelengths for the *Spitzer* 3.6, 4.5, 8.0, 24, 70, and 160 μm bands and include synthetic photometry points at 13, 24, and 33 μm created from the IRS spectra. No color corrections have been applied; see text. Error bars are indicated but generally are smaller than the plotted points. Open symbols are *IRAS* measurements. Thin solid curves are single-temperature blackbody fits to the 33–70 μm color excess (*dashed curve*) summed with the photosphere (*thick solid curve*). In all cases, the observed flux densities (connected by dotted lines) are broader than a single-temperature blackbody and indicate cooler outer disk material, as well as warmer inner disk material in addition to material at the distance of the plotted fiducial single temperature. At the same time, the shortest wavelength near-infrared bands are photospheric, indicating that the disks do not extend inward of about 0.2–0.5 AU, with the excesses beginning by $\sim$8 μm. Detailed modeling of these sources will be presented elsewhere (e.g., S. Cortes et al. [2008, in preparation] for PDS 66). [*See the electronic edition of the Journal for a color version of this figure.*]

4.1. *Single-Temperature Models*

The observed excesses are most prominent at wavelengths around 70 μm, as illustrated in Figure 7. High-precision *Spitzer* photometry at shorter wavelengths generally samples the Wien side of the blackbody function. FEPS data include IRS spectrophotometry that represents a higher resolution sampling of the SED from 5 to 35 μm; these data allow accurate determination of the wavelength at which the departure from a photospheric model occurs, as presented in J. M. Carpenter et al. (2008a, in preparation). Here we use simple blackbody fitting to color temperatures (including synthetic IRS 13 μm and IRS 33 μm bands). Many of the debris disk sources are detected at 160 μm as well, providing information past the excess peak (Rayleigh-Jeans regime).

4.1.1. *Dust Temperature*

We calculate color temperatures $T_{\rm color}$, defined as the blackbody temperature required to fit the flux ratios in the excess above the photosphere, at 24–33, 33–70, and 70–160 μm. We also tabulate 13–33 μm color temperatures, which we choose over 13–24 μm for two reasons: first, data from a single instrument are used, avoiding systematics due to calibration; and second, in practice the 13–33 μm flux ratio provides a tighter upper limit on the maximum color temperature than the 13–24 μm flux ratio. The color temperatures are considered measured values when the excess is $\geq 2\,\sigma$ at both the shorter and longer wavelengths and limits when the excess is $<2\,\sigma$ at one of the two wavelengths but $\geq 2\,\sigma$ at the other. For example, some stars have 33 μm photometry consistent with purely photospheric emission; in calculating a 33–70 μm color temperature we are assuming, therefore, that the infrared excess begins just longward of 33 μm. In such cases we determine the maximum color temperature from the minimum wavelength of infrared excess onset. The significance values include total uncertainty on

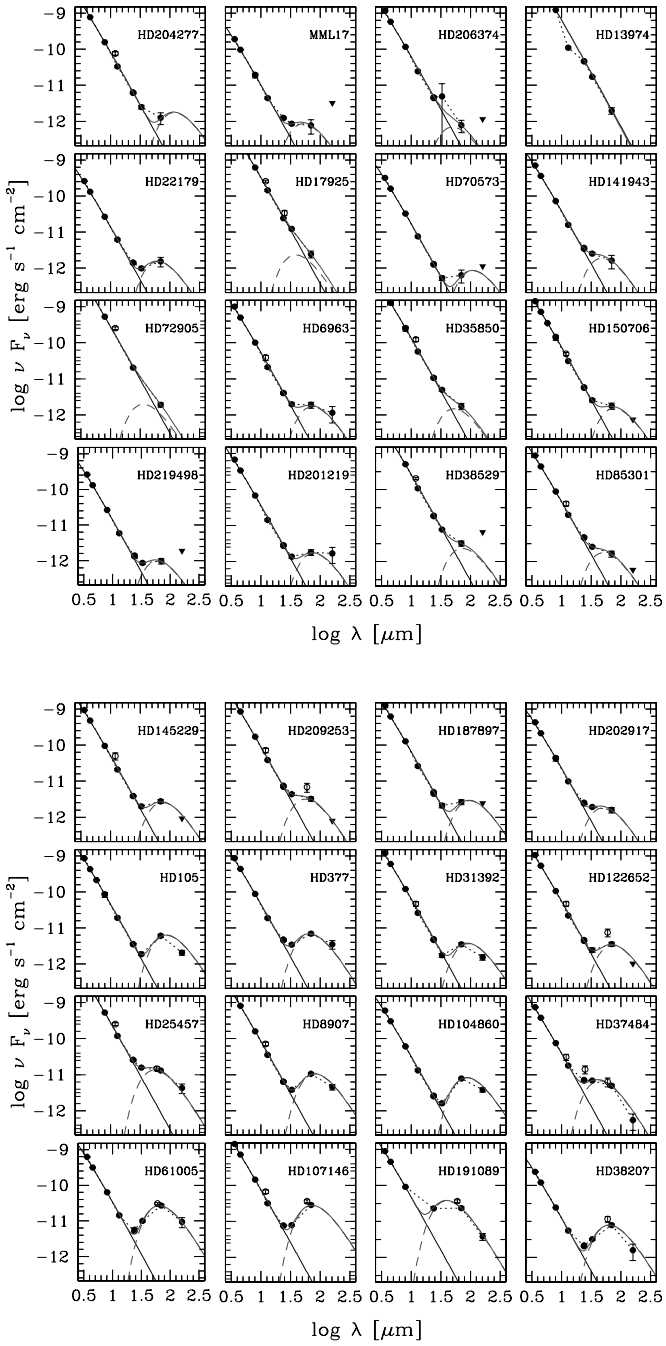

FIG. 7.—SEDs for the 70 μm excess sources in the FEPS debris disk sample, having >3 σ significance in 25 cases and >2 but <3 σ significance in six cases. Objects are ordered most significant excess at bottom left to least significant excess at top right (see Table 3). Symbols and lines are as in Fig. 6. Single-temperature blackbody fits are generally to the 33–70 μm color excess and slightly underpredict the 24 μm excess while overpredicting the 160 μm excess (when detected). The fits are to the 24–70 μm color excess for HD 191089 and HD 72905 due to the absence of 33 μm photometry and for HD 206374 due to the poor quality of IRS spectrum just around 33 μm. [*See the electronic edition of the Journal for a color version of this figure.*]

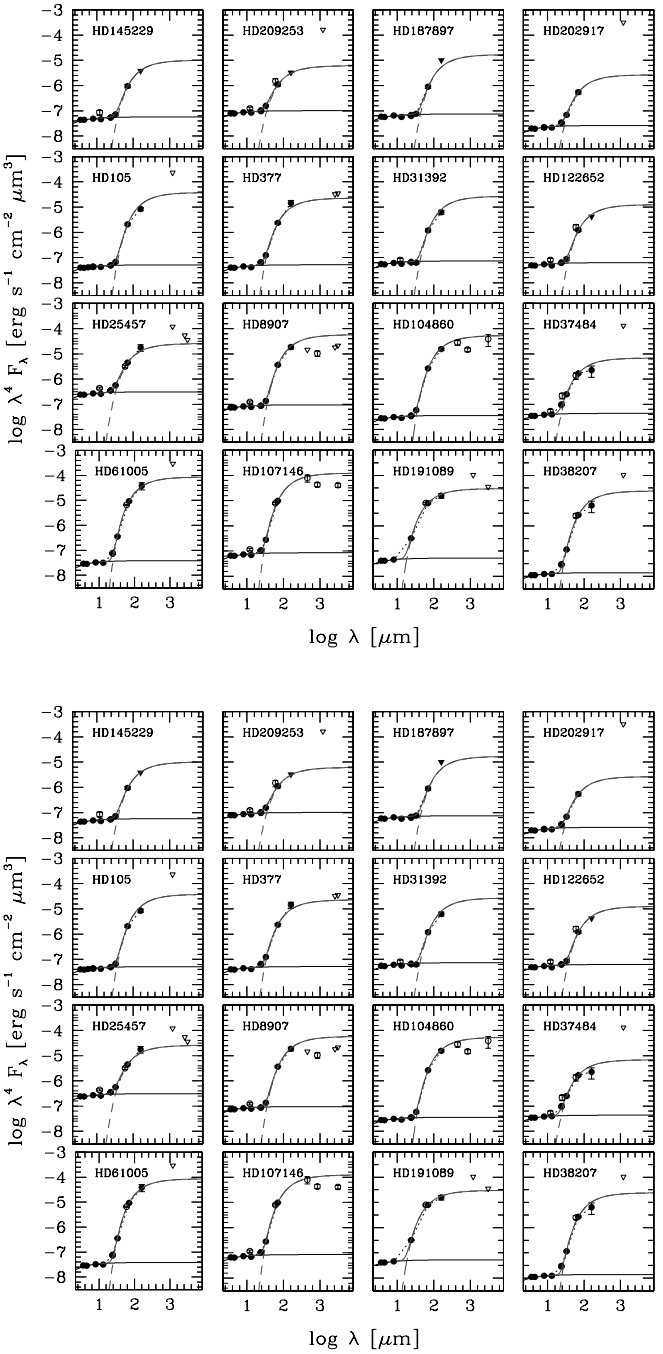

FIG. 8.—SEDs for the same *Spitzer* 70 μm excess sources of Fig. 7 now plotted in units such that the long-wavelength Rayleigh-Jeans regime of a blackbody function is flat. In addition, the abscissa has been extended to millimeter wavelengths so as to demonstrate the need for models more complex than single-temperature blackbodies to match available long-wavelength photometry. In cases where the flux is overpredicted, this is generally achieved using modified blackbodies for which the temperatures would be similar to those derived from our mid-infrared fitting, but the far-infrared to millimeter slope could be used to constrain the spectral index β. [*See the electronic edition of the Journal for a color version of this figure.*]

the photometry (internal measurement plus calibration error) and the formal uncertainty on the photosphere (2%–3% is typical).

The various $T_{\rm color}$ fits are given in Table 4, along with the χ^2_ν values resulting from a fit of a blackbody having this temperature to the broader excess SED from 13 to 160 μm; the number of data points used to calculate reduced χ^2 is 4 or 5 in almost all cases. Mean (median) color temperatures for 24–33, 33–70, and 70–160 μm are 101.6 (92.5), 73.1 (59), and 61.6 (56.5) K, respectively, including the limits, which implies that the mean (median) values above are also upper limits. As cited in the MIPS Data Handbook (Table 3.11 in ver. 3.2), color corrections for source temperatures of 50–100 K are in the range 2%–11% depending on photometric band (24, 70, or 160 μm). The color temperatures calculated for color-corrected photometry are different by only 0.5–3 K from those calculated without the inclusion of color terms; in most cases these are within or comparable to the formal errors on the color temperature as calculated from the photometric/photospheric uncertainties (see Table 4). As our blackbody analysis is meant to be illustrative of the dust properties characterizing our debris disk sample rather than definitive, we have not applied color corrections to individual sources. Given the systematic differences in color temperature across the SED of some of the excesses, this seems prudent.

As is evident from the table, short-wavelength excesses are rare among the FEPS sources with 70 μm excess. None (among the debris disk sample) exhibit <8 μm excess within our errors. Only HD 202917 exhibits possible 13 μm excess at a level >2 σ (just 2.2 σ). All other 13–33 μm color temperatures in Table 4 are upper limits and produce very poor χ^2_ν values when used to fit the overall energy distribution as might thus be expected. At 24 μm, approximately $\frac{1}{2}$ of the 70 μm excess sources are also in excess, while at 33 μm approximately $\frac{2}{3}$ of the 70 μm excess sources are also in excess; thus, about $\frac{1}{2}$ of the 24–33 μm and $\frac{1}{3}$ of the 33–70 μm color temperatures are upper limits.

In some cases the color temperatures derived from the flux ratios at different wavelengths agree quite well, for example, HD 104860, HD 8907, and HD 209253. In other cases, such as HD 377, HD 38207, and HD 85301, the three color temperatures are very discrepant and none produce an adequate fit to the overall SED. The general trend among our sources is of cooler color temperatures inferred from the longer wavelength data and hotter temperatures derived from the shorter wavelength data.[13] Furthermore, J. M. Carpenter et al. (2008a, in preparation) find that the fits to 5–35 μm IRS data underpredict the 70 μm excess by >3 σ for $\frac{3}{4}$ of the sources for which data are available. The systematic discrepancies are suggestive of a physical effect rather than resulting from data errors; further, the phenomenon of inconsistent color temperatures is not due to the presence of prominent spectral features, as none are detected in our S/N $>$ 30 spectra from IRS. It should also be noted that we would expect the same blackbody that fits the shorter wavelength points to also fit the longest wavelength 160 μm point only if the grains are as large as 20 μm; smaller grains that produce blackbody times emissivity ($Q_\lambda < 1$) would underpredict this flux density.

We offer an explanation for the temperature discrepancies in terms of multitemperature dust located over a range of radii in the next section. In the remainder of this section we interpret the color temperatures derived from the 33–70 μm flux ratio as the fiducial, characteristic, dust temperature ($T_{\rm dust}$) that represents the bulk of the excess SED. In several cases noted in Table 4 (e.g., HD 22179, HD 35850, HD 37484, HD 85301, MML 17, in addition to HD 141943 and HD 209253) the χ^2_ν values resulting from the (hotter) 24 μm/33 μm color temperature models are <2 and are comparable to or, in some cases, better than those for the 33 μm/70 μm color temperature models. In one case (HD 31392) we adopt the 70 μm/160 μm color temperature model.

[13] Of note is that the (modified) blackbody dust temperatures fitted by J. M. Carpenter et al. (2008a, in preparation) to 5–35 μm IRS spectrophotometry (as opposed to just the synthetic 13 and 33 μm "photometry" points used here) are in every case intermediate between those of our 13–33 and 24–33 μm values.

TABLE 4

COLOR TEMPERATURES AND REDUCED χ^2 VALUES

Source	T_{color}(13 μm/33 μm)	T_{color}(24 μm/33 μm)	χ^2_ν(13−160 μm)	T_{color}(33 μm/70 μm)	χ^2_ν(13−160 μm)	T_{color}(70 μm/160 μm)	χ^2_ν(13−160 μm)
Tier 1 Debris Disks (Excess $S/N_{70\,\mu m} \geq 3$)							
HD 105	<212	93^{+50}_{-28}	23.9	46^{+3}_{-3}	2.97	57^{+12}_{-8}	13.0
HD 377	<69	93^{+17}_{-13}	13.2	58^{+3}_{-3}	3.92	46^{+12}_{-7}	14.0
HD 6963	...	<76	2.76	56^{+9}_{-8}	0.36	42^{+25}_{-9}	1.13
HD 8907	<123	<59	14.0	48^{+3}_{-3}	0.08	50^{+8}_{-6}	0.24
HD 22179	<175	100^{+22}_{-16}	1.92	61^{+9}_{-6}	4.14	...	...
HD 25457	<157	106^{+30}_{-21}	15.0	70^{+5}_{-5}	1.41	58^{+23}_{-10}	6.67
HD 31392	...	...	...	<47	0.80	49^{+10}_{-6}	1.02
HD 35850	<265	120^{+132}_{-42}	1.59	82^{+19}_{-13}	0.65	...	...
HD 37484	<149	101^{+11}_{-9}	2.19	86^{+6}_{-6}	2.87	291^{+10}_{-194}	>100
HD 38207	<133	76^{+6}_{-5}	12.5	59^{+3}_{-2}	7.9	88^{+212}_{-29}	>100
HD 38529	...	...	...	<48	0.10	>27	3.41
HD 61005	<111	68^{+5}_{-4}	7.7	58^{+3}_{-2}	3.93	57^{+23}_{-10}	7.32
HD 72905	...	...	...	<103[a]	...	...	...
HD 85301	<139	127^{+49}_{-27}	2.17	76^{+11}_{-8}	2.57	>53	10.4
HD 104860	<124	<67	29.6	45^{+3}_{-3}	0.55	47^{+6}_{-4}	0.58
HD 107146	<122	72^{+9}_{-8}	25.1	52^{+2}_{-2}	3.34	...	...
HD 122652	...	<71	4.50	55^{+7}_{-7}	0.53	>63	1.61
HD 145229	<169	<82	6.41	54^{+5}_{-5}	0.37	>56	1.52
HD 150706	<181	<91	2.78	58^{+11}_{-11}	0.12	>48	0.42
HD 187897	...	<92	8.40	<45	0.28	>36	0.33
HD 191089	...	...	...	<92[a]	0.41	113^{+113}_{-32}	>100
HD 201219	...	<83	4.24	53^{+7}_{-7}	0.53	36^{+15}_{-6}	1.56
HD 202917	185^{+33}_{-33}	101^{+16}_{-12}	2.99	77^{+9}_{-7}	4.18	...	...
HD 209253	<211	77^{+27}_{-19}	0.86	70^{+8}_{-6}	0.59	>68	7.05
HD 219498	...	95^{+29}_{-19}	3.44	65^{+7}_{-6}	1.44	>29	11.4
Tier 2 Debris Disks (Excess $S/N_{70\,\mu m} \geq 2$ and <3)							
HD 17925	...	...	...	110^{+57}_{-25}	0.32	...	...
HD 70573	...	...	...	<47	0.88	>29	1.38
HD 141943	<167	90^{+18}_{-13}	0.35	81^{+27}_{-12}	0.58	...	...
HD 204277	...	...	...	<50	0.14	...	...
HD 206374	...	...	...	<74[a]	0.46	>29	0.20
MML 17	<153	120^{+27}_{-18}	0.70	74^{+22}_{-10}	6.23	>24	28.3

NOTES.—Temperatures are in K. Uncertainties are based on formal uncertainties in flux density ratios and are rounded to the nearest degree. Upper limits are noted when the shorter wavelength from which the color temperature is calculated is in excess of the photosphere by $<2\,\sigma$. Lower limits are noted in some instances at 70 μm/160 μm and are based on 2 σ upper limits to 160 μm flux densities. The χ^2 values are calculated for usually four to five bandpasses within 13–160 μm, which requires efficient grains over a factor of 10 in wavelength for good fits.

[a] For HD 191089, HD 72905, and HD 206374 the quoted color temperature between 33 and 70 μm is actually from 24 to 70 μm due to lack of or poor quality IRS data at 33 μm. The quoted values are considered upper limits to the 33 μm/70 μm color temperature but are upper limits to the measured 24–70 μm color temperature only in the case of HD 206374.

TABLE 5

DUST PROPERTIES

SOURCE	T_{dust}[a] (K)	R_{inner} (AU)	$\log(L_{dust}/L_*)$	$\log(M_{dust,min}/M_\oplus)$	$\tau_{collisions}/\tau_{P\text{-}R}$ Assuming $\alpha = 0$ at R_{inner}	$\tau_{collisions}/\tau_{P\text{-}R}$ Assuming $\alpha = -1$ at 200 AU
Tier 1 Debris Disks (Excess $S/N_{70\,\mu m} \geq 3$)						
HD 105	46	42	−3.5	−3.1	0.004	0.4
HD 377	58	23	−3.4	−3.4	0.004	0.3
HD 6963	56	18	−4.0	−4.3	0.010	0.6
HD 8907	48	49	−3.6	−3.1	0.008	0.9
HD 22179	61[b]	31	−3.6	−3.4	0.010	0.8
HD 25457	70	23	−4.0	−4.1	0.027	1.8
HD 31392	49[c]	24	−3.8	−3.8	0.005	0.3
HD 35850	82	15	−4.5	−4.9	0.086	4.8
HD 37484	86[b]	20	−3.5	−3.7	0.018	1.2
HD 38207	59	51	−3.0	−2.4	0.005	0.5
HD 38529	<48[d]	86	−4.6	−3.5	0.150	30.7
HD 61005	58	17	−2.6	−2.9	<0.001	<0.1
HD 72905	103	7	−4.7	−5.8	0.110	4.2
HD 85301	76[b]	11	−3.9	−4.6	0.012	0.6
HD 104860	46[e]	42	−3.2	−2.8	0.002	0.2
HD 107146	52	30	−3.1	−2.9	0.001	0.1
HD 122652	55	31	−3.9	−3.7	0.014	1.1
HD 145229	54	26	−3.9	−3.9	0.010	0.8
HD 150706	58	23	−4.3	−4.4	0.027	1.9
HD 187897	<45[d]	43	−4.0	−3.6	0.014	1.4
HD 191089	92	16	−2.8	−3.2	0.004	0.2
HD 201219	53	23	−3.9	−4.0	0.007	0.5
HD 202917	77[b]	11	−3.6	−4.3	0.005	0.3
HD 209253	70	20	−4.1	−4.3	0.030	1.9
HD 219498	65	41	−3.7	−3.3	0.027	2.5
Tier 2 Debris Disks (Excess $S/N_{70\,\mu m} \geq 2$ and <3)						
HD 17925	110	4	−4.4	−6.0	0.036	1.0
HD 70573	41[e]	35	−4.0	−3.7	0.007	0.6
HD 141943	85[e]	18	−3.8	−4.1	0.014	1.7
HD 204277	<50[d]	43	−4.6	−4.1	0.074	7.2
HD 206374	<74[d]	12	−4.5	−5.1	0.042	2.0
MML 17	74[b]	23	−3.7	−3.7	0.018	1.2

[a] Adopted T_{dust} from among values in Table 4, typically the 33 μm/70 μm color temperature, but other cases as footnoted.

[b] While the adopted T_{dust} is from the 33 μm/70 μm flux ratio, the hotter 24 μm/33 μm value produces a lower χ^2 to the overall SED; see Table 4. In these cases, contrary to the situation of footnote d, the R_{inner}, L_{dust}/L_*, and $M_{dust,min}/M_\oplus$ may be lower than we quote while $\tau_{collisions}/\tau_{P\text{-}R}$ may be higher, all in the blackbody assumption.

[c] Adopted T_{dust} is from the 70 μm/160 μm flux ratio rather than 33 μm/70 μm.

[d] In the cases of temperature upper limits, R_{inner}, L_{dust}/L_*, and $M_{dust,min}/M_\oplus$ are all minimum values while $\tau_{collisions}/\tau_{P\text{-}R}$ are maxima.

[e] Adopted T_{dust} is an average of consistent values from Table 4.

4.1.2. *Dust Location and Luminosity*

For the assumed blackbody case, simple radiative balance suggests

$$(R_{\rm dust}/50\ {\rm AU}) = 0.62(L_*/L_\odot)^{1/2}(T_{\rm dust}/50\ {\rm K})^{-2},$$

where $R_{\rm dust}$ is the radial distance of the dust from the star, $T_{\rm dust}$ is the dust temperature, and L_* is the stellar luminosity.[14] With L_* from the Kurucz model and $T_{\rm dust}$ assumed to be the color temperature of the infrared excess as derived above, the dependent variable $R_{\rm dust}$ can be calculated. The dust luminosity, $L_{\rm dust}$, is then estimated using $T_{\rm dust}$, $R_{\rm dust}$, and the Stefan-Boltzmann relation. For single-temperature blackbody emission this is a more precise method than trapezoidal integration of the measured excess flux densities, which results in only a minimum value for $L_{\rm dust}$. Finally, $f = L_{\rm dust}/L_*$, the fractional infrared excess, is derived.

Table 5 lists the inner radii corresponding to the assumption of large (relative to wavelength) grains along with corresponding values of fractional dust excess. Formal error propagation from the dust temperature and stellar luminosity uncertainties into those for the dust radii, $R_{\rm dust}$, reveals uncertainties of ~10%–35%, but we emphasize that these radii are only notional minimum values derived under the strong assumption of blackbody grains. They are *lower limits* as smaller grains would achieve the estimated temperatures at larger radii.[15] The uncertainties on dust luminosity, f, are more complex to quantify.

In the pure blackbody assumption, the maximum contribution at 70 μm (if in νF_ν) comes from dust at $T = 3675/71.4 = 51.5$ K. For a dust emission peak near 70 μm, the factor $h\nu/kT$ in the blackbody flux density equation is constant, and from further consideration of the contrast with the Rayleigh-Jeans tail of the underlying stellar SEDs, one finds a minimum value for f

$$(L_{\rm dust}/L_*)_{\rm minimum} = 10^{-5}(5600/T_*)^3\left(F_{70,\rm excess}/F_{70,*}\right).$$

For a dust excess peaking shortward or longward of 70 μm, the resulting dust luminosity is higher for the same monochromatic excess; this is illustrated in Figure 9, which shows the run of $L_{\rm dust}/L_*$ with $T_{\rm dust}$ for constant values of the measured quantity $F_{70,\rm excess}/F_{70,*}$. In many cases we have, rather than a measurement of $T_{\rm dust}$, only a limit on $T_{\rm dust}$. This leads to a limit on f, which is an upper or lower limit depending on the value and sign of the $T_{\rm dust}$ limit. For solar-luminosity stars, the dust temperature maxima that are much larger than 51.5 K result in inferred f-values that are likely upper limits, while for dust temperature maxima smaller than 51.5 K the f-values are definitely *lower* limits, all in the blackbody situation.

In practice, the values of f derived in the blackbody scenario from the inferred $T_{\rm dust}$ are in fact quite close to the f minima for an assumed blackbody radiation peak at 70 μm, within 0.1–0.2 dex in most cases.

Returning now to the case in which the grains are nonblackbody (i.e., smaller) and the dust inner radii ($R_{\rm dust}$) inferred via the blackbody assumption are thus lower limits, the dust cross-sectional areas (A) are then also lower limits. In other words, if the dust is actually smaller than the assumed blackbody size, in order to achieve the same $T_{\rm dust} = T_{\rm color}$, the observed 70 μm flux density would require more total dust area by a factor $\lambda/2\pi a = 11.4\ \mu{\rm m}/a$. Dust luminosity scales with $T_{\rm dust}^4 \times Q$ but also with A where $A/R_{\rm dust}^2 \ll 1$ for optically thin emission. In contrast to the pure blackbody case above, here $f = f_{\rm bb}(T_{\rm dust}/51.5\ {\rm K})$. Thus, dust temperature maxima larger than 51.5 K result in f-values that are larger than blackbody, and the assumed blackbody case produces a lower limit on f, while for dust temperature maxima smaller than 51.5 K, the f-values are smaller than blackbody and the assumed blackbody case is an upper limit on f.

4.1.3. *Dust Mass*

The dust mass, $M_{\rm dust}$, can be determined by assuming a grain material density and estimating an average grain size to compute the mass per particle, which is then multiplied by the number of particles. We consider 2.5 g cm^{-3} an appropriate average density for silicate dust, although we acknowledge a 50% range in the values inferred among asteroids and asteroidal IDPs. For the grain size there are several options depending on the dominant physical process that is controlling the removal of grains from the dust disk. We assume that the production of dust grains is through the collisional cascade of larger parent bodies, although this detail is not important just yet.

One option is to use a 10 μm grain size. For efficient (i.e., blackbody) emission at a wavelength of 70 μm, the radiative absorption and emission efficiency factors Q_λ(abs, emis) are close to unity, implying for $1 < 2\pi a/\lambda$ grains larger than $a \approx 10$ μm. Such large sizes are also consistent with, although not necessarily demanded by, a lack of observed spectral features in the shorter wavelength IRS data, which for our sources generally trace well the stellar photospheric or photosphere-plus-dust continuum levels (Bouwman et al. 2008; J. M. Carpenter et al. 2008a, in preparation). Although the details of this argument depend on the temperature structure of the disk, emission from hot dust of any size, including small amounts of moderate-sized (~1 μm) equilibrium silicates or very small (<0.05 μm) nonequilibrium grains/polycyclic aromatic hydrocarbons, is not evident.

A second option is to estimate the average grain size from the minimum grain size expected to survive in a dust disk in which stellar radiation pressure removes grains not balanced by gravitational (and P-R drag) forces working to keep them in orbit about the star (i.e., $\beta = 0.5$). Based on Burns et al. (1979) and Artymowicz (1988), the minimum grain size in a (gas-poor) disk is

$$\frac{a_{\rm min}}{\mu{\rm m}} = 0.52\frac{2.5\ {\rm g\ cm^{-3}}}{\rho}\frac{L_*/L_\odot}{(M_*/M_\odot)(T_*/5780)}$$

[14] Allowing for smaller, nonblackbody grains with emissivity $Q_\lambda \propto \lambda^{-\beta}$ (β is in the range 0.5–2, whereas $\beta = 0$ for blackbody grains) would increase the grain temperature at a given distance from the star. This would mean that derived dust radii would increase relative to the blackbody case having

$$\frac{L_*}{L_\odot} = 2.62\left(\frac{R_{\rm dust}}{50\ {\rm AU}}\right)^2\left(\frac{T_{\rm dust}}{50\ {\rm K}}\right)^4$$

for the same fitted dust temperature. Specifically, for graybody grains that are efficient absorbers and inefficient emitters

$$\frac{L_*}{L_\odot} = 3.47\times10^{-2}\left(\frac{R_{\rm dust}}{50\ {\rm AU}}\right)^2\left(\frac{T_{\rm dust}}{50\ {\rm K}}\right)^5\left(\frac{\langle a\rangle}{\mu{\rm m}}\right),$$

and for those that are inefficient absorbers as well as inefficient emitters, as is the case for very small ISM-like grains,

$$\frac{L_*}{L_\odot} = 2.10\times10^{-3}\left(\frac{T_*}{T_\odot}\right)^{-1.5}\left(\frac{R_{\rm dust}}{50\ {\rm AU}}\right)^2\left(\frac{T_{\rm dust}}{50\ {\rm K}}\right)^{5.5},$$

derived from formulae in Backman & Paresce (1993).

[15] For a typical source such as HD 105, the formal uncertainty in the fitted dust temperature (~10%) corresponds to an uncertainty of ~20% in the dust inner radius estimated under the assumption of blackbody emission from the equation above (with a best-fit value of 42 AU listed in Table 5). Under different assumptions regarding the nature of the emitting grains, this same temperature would correspond to much larger radii of ~400 AU (efficient absorbers and inefficient emitters with a mean grain size of 0.95 μm) or >1000 AU for ISM-like grains smaller than the blowout size (0.59 μm).

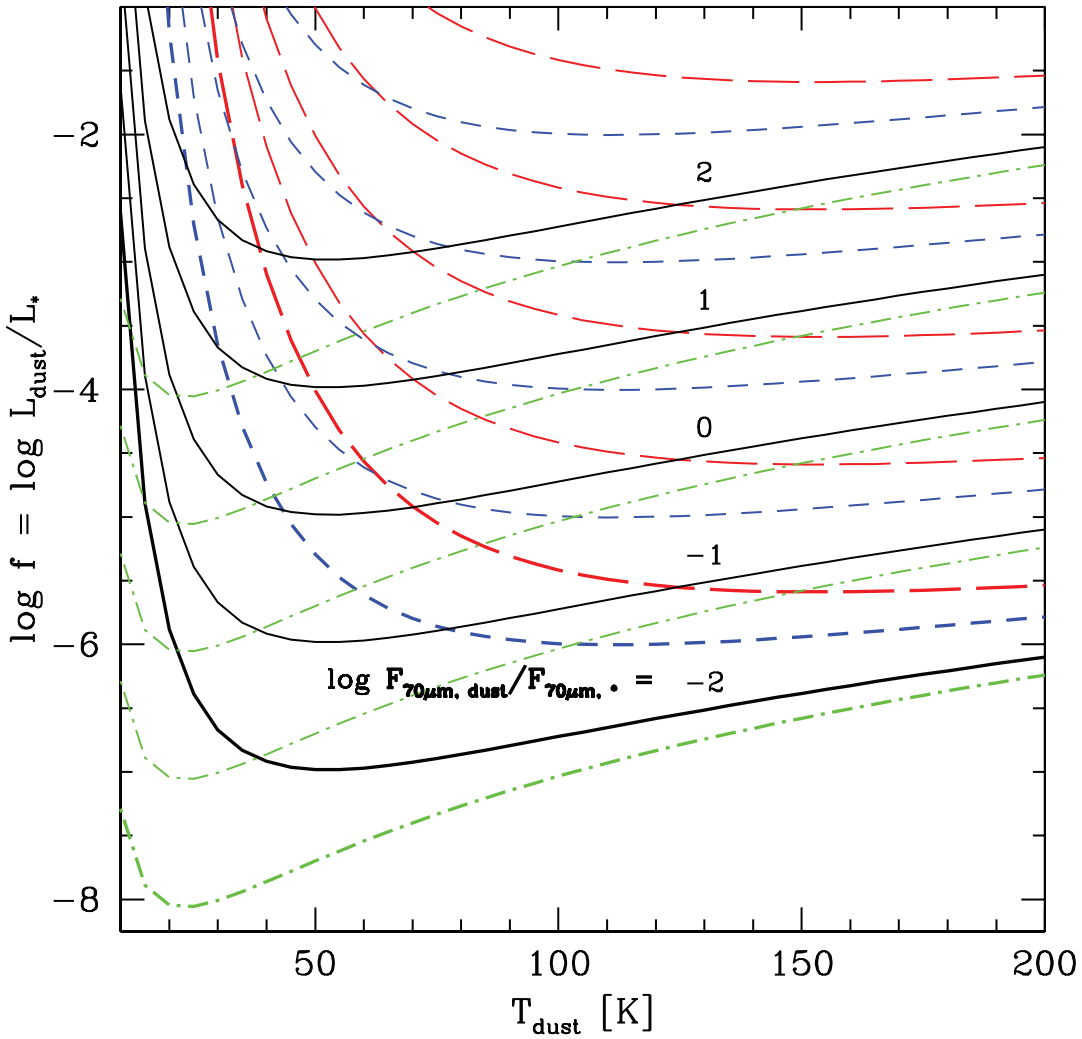

FIG. 9.—Fractional infrared excess as a function of $T_{\rm dust}$ for different values of the observed quantity $F_\lambda({\rm dust})/F_\lambda(*)$ at $\lambda = 70$ μm (*black*). Comparable curves are shown for the same fractional excess values at $\lambda = 160$ μm (*green*), $\lambda = 33$ μm (*blue*), and $\lambda = 24$ μm (*red*). Note that at the same monochromatic contrast level the fractional luminosity of the excess to which we are sensitive goes down toward longer wavelengths (along with the instrumental capability to achieve those monochromatic contrast levels). The curves also become broader toward shorter wavelengths, which can probe a wider dust temperature range to the same fractional excess luminosity level. Observations at 70 μm and longer are uniquely suited to detection of Kuiper Belt–like dust distributions. The FEPS observations discussed here detect primarily 50–100 K dust with $\log f = -5$ to -3.

[which can be scaled as (1 + albedo)/1.1 if an alternate is desired to the assumed 0.1 albedo of solar system silicate dust]. Smaller grains are blown out, while bigger grains are retained and subject to collisions with other grains in a sufficiently dense disk. Among our sample stars, the range in the predicted $a_{\rm min}$ is 0.3–2.5 μm. The average grain size $\langle a \rangle$ is close to the minimum grain size, $(5/3)a_{\rm min}$ for a distribution going as a power law with exponent -3.5; this is the appropriate exponent for the interstellar distribution (Mathis et al. 1977) although extrapolated in this application to larger grain sizes than typically populate the ISM, as well as to a self-similar infinite collisional cascade[16] (Dohnanyi 1969; Durda & Dermott 1997). In this case the typical grain size is thus a few microns.

A third option would be to assume that corpuscular drag (due to the effects of stellar winds on orbiting dust particles, rather than to those of stellar radiation as in P-R drag) is responsible for grain removal. Neither P-R drag nor corpuscular drag effects appear to dominate in our disks, however (see § 5.3), and so we do not consider this case in detail.

Dust masses, $M_{\rm dust}$, can be calculated from the assumed grain density, the grain size, and the total number of particles at that size, which we estimate by considering the fractional infrared luminosity ($L_{\rm dust}/L_*$) divided by the fractional solid angle intercepted by a single dust grain ($\pi a^2/4\pi R_{\rm dust}^2$). For simplicity, we consider only the average grain size $\langle a \rangle$. Because any smaller grains that are present provide more surface area, and hence opacity, we thus calculate minimum dust masses. The dust mass is thus

$$M_{\rm dust} > \frac{16}{3}\pi\left(\frac{L_{\rm dust}}{L_*}\right)\rho\langle a\rangle R_{\rm dust}^2$$

[16] For collisionally dominated disks, such as we think dominate our sample, it can be argued that the number of small grains at the inner edge of the debris disk is actually *higher* than predicted by such a power law since those just below the blowout size are preferentially removed via radiation pressure and therefore not available to collide with those just above the blowout size (e.g., Krivov et al. 2000), leading to a "wavy" size distribution (e.g., Thébault et al. 2003, 2007), with more grains at about $1.5a_{\rm min}$ and fewer grains at $10a_{\rm min}$–$50a_{\rm min}$, relative to the Dohnanyi distribution. We do not consider such complexity here. For P-R–dominated disks, on the other hand, there may be *fewer* small grains at the inner edge and overall, since a shallower power law may be more appropriate as in the solar system, where $n(a) \propto a^{-2.4}$ (e.g., Fixsen & Dwek 2002).

TABLE 6
Extended Disk Models

Source	ΔT_{color}[a] (K)	R_{inner}[b] (AU)	R_{outer}[c] (AU)	σ_0[d]	rms Deviation[e]
HD 85301	51 ± 15	0.7	>200	6.63×10^{-5}	0.12
HD 105	47 ± 39	36.8	38	2.80×10^{-2}	1.27
MML 17.....	47 ± 28	1.9	>200	1.24×10^{-4}	0.15
HD 22179	39 ± 20	6.4	>200	1.66×10^{-4}	0.66
HD 377	36 ± 15	8.5	137	3.15×10^{-4}	1.05
HD 25457	36 ± 26	5.0	92	8.50×10^{-5}	0.44
HD 219498	31 ± 25	11.6	>200	1.57×10^{-4}	0.40
HD 202917	24 ± 16	2.5	40	2.08×10^{-4}	0.07
HD 107146	20 ± 9	13.6	>200	9.52×10^{-4}	0.93
HD 38207	17 ± 6	21.2	130	1.15×10^{-3}	1.22
HD 37484	15 ± 12	8.2	34	4.35×10^{-2}	0.87
HD 61005	10 ± 5	8.6	41	3.35×10^{-3}	0.35
HD 141943	9 ± 25	8.6	40	1.95×10^{-4}	0.01

Notes.—Included in this table are all sources from Table 4 with $\chi^2_\nu > 1.2$ from the 33 μm/70 μm flux ratio. In addition, we present for comparison a disk model of HD 141943, which is well fitted by a single-temperature blackbody matched to the 33 μm/70 μm flux ratio. List is sorted inversely by ΔT_{color}.

[a] ΔT_{color} is the difference between the 24 μm/33 μm and 33 μm/70 μm color temperatures in Table 4, i.e., the temperature range that must be explained in the extended disk model. Quoted error is the rms of the individual color temperature errors, ignoring the covariance term suggested by the appearance of the 33 μm flux density in both color temperatures; asymmetric errors have been simply averaged.

[b] R_{inner} is the inferred inner disk radius.

[c] R_{outer} is the inferred outer disk radius. A value of 200 means that the outer boundary is indeterminate, even for $\alpha = 0$ models; for the fits it is held constant and only R_{inner} and σ_0 are varied.

[d] The σ_0 is the inferred surface density at $R = R_{inner}$, constant with radius in these $\alpha = 0$ models. The units of σ are dimensionless, in cm^2 of grain cross section per cm^2 of disk area, distinguished from the usual definition of Σ_0, which is in per cm^2 of disk area. Note that high values are required in the narrower disk cases.

[e] The rms deviation of the SED from the constant surface density blackbody disk having R_{inner}, R_{outer}, and σ_0. This is the square root of the summed squared deviations divided by number of points (usually 4 from 24–160 μm).

or

$$\frac{M_{dust}}{M_\oplus} > 1.59 \times 10^{-4} \left(\frac{L_{dust}}{L_*}\right) \left(\frac{\rho}{2.5 \text{ g cm}^3}\right) \left(\frac{\langle a \rangle}{\mu\text{m}}\right) \left(\frac{R_{dust}}{\text{AU}}\right)^2$$

(see Backman & Paresce 1993; Jura et al. 1995).

The results of our simple modeling can be found in Table 5, where we have adopted from the above discussion a value of 10 μm for $\langle a \rangle$. The uncertainty in the dust masses is significant, not only because of the linear scaling with assumed $\langle a \rangle$, but also because our values of R_{dust} are always lower limits in the blackbody assumption.

A separate point is that much mass can be hidden in larger grains, pebbles, and rocks that, given their ratio of surface area to mass, do not radiate strongly at even the longer *Spitzer* wavelengths. For an assumed grain size distribution going as $n(a) \propto a^{-3.5}$, the mass in larger grains can be accounted for, yielding a total mass

$$M_{total} = M_{dust,min} \sqrt{a_{max}/a_{min}}$$

(for a more general formula for an arbitrary particle size distribution see Wyatt et al. 2007). Because a_{max} generally is not known, we quote *dust* masses calculated for the average grain size $\langle a \rangle$ only, which in our case is relatively close to a_{min}.

4.2. *Multitemperature Disk Models*

For many of our 70 μm excess detections, single-temperature blackbody models fitted to the excess emission do a poor job, according to the χ^2_ν values in Table 4, of reproducing the observed SEDs. We identify for further investigation those sources with $\chi^2_\nu > 1.2$ in the 33–70 μm color temperature fit. The probability that such high χ^2_ν values are a good fit to the data is <25%. There are 12 systems, more than $\frac{1}{3}$ of our excess sample, which we propose in Table 6 as having evidence for material with (at least) two different temperatures.

For these sources, we quantify the disparity in the color temperatures derived from the 24–33 μm versus the 33–70 μm excess flux density ratios in the second column of Table 6. We illustrate in Figure 10 the color temperatures for all sources in our 70 μm–selected excess sample having 33 and 24 μm excesses as well. Regardless of the temperature, no single-temperature model can fit simultaneously the measured 24, 33, and 70 μm excesses for many (those listed in Table 6) of these sources. So-called modified blackbodies [or graybodies, having optical depth $\tau = \tau_0(\lambda/\lambda_0)^{-\beta}$; $\beta = 0$ for a $\tau > 1$ blackbody] that represent analytically the case of inefficient small (compared to the wavelength of observation) grain emission are also illustrated in Figure 10. Modified blackbody models are in even less agreement with the data, which suggests that other effects (perhaps dust geometry) trump any inaccuracies in our treatment of grain properties. Observatory calibration errors of a systematic nature could potentially improve the agreement in terms of fitting the mean of the distribution of points. However, such errors would have to be large, about 50% too high for either of MIPS-24 or MIPS-70 and about 30% too low for IRS, much larger than the current calibration precision. We emphasize based on Figure 10 and Table 6 that for any individual source the disagreement of the data and the single-temperature blackbody is generally only a 1–2 σ effect and any conclusion would be marginal at best. However, we interpret the systematic trend as indicative of a real effect that characterizes the ensemble of stars.

We are thus motivated to consider multitemperature dust models. While primordial gas- and dust-rich disks offer ample evidence for multitemperature disks (e.g., Dullemond et al. 2007), it is unusual for debris disks to exhibit SEDs with emission at a wide range of temperatures.

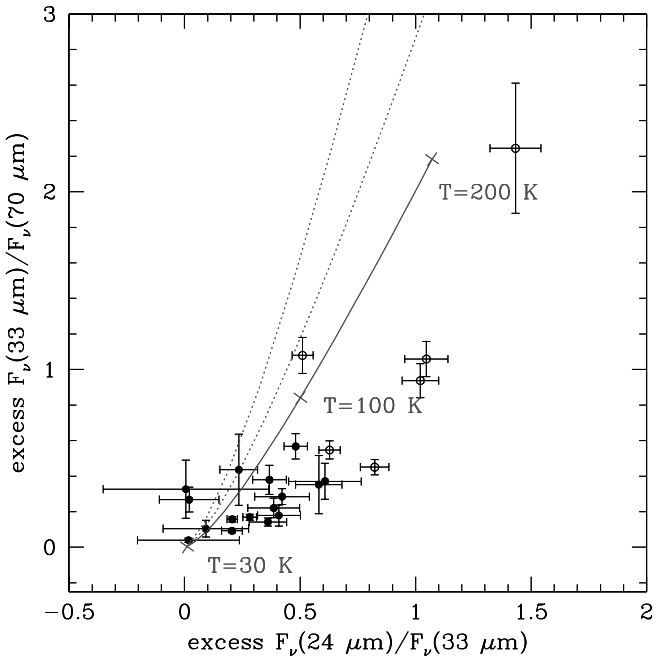

FIG. 10.—Demonstration of the failure of single-temperature blackbodies to explain simultaneously the observed 24, 33, and 70 μm photometric excesses. Points with errors represent excess flux density ratios, that is, observed flux density ratios corrected for their underlying stellar photospheric contributions. Error bars include the observational errors but no error in the photosphere. Filled symbols represent the debris disks of Fig. 7, while open symbols represent the primordial disks of Fig. 6. The solid line is a blackbody temperature sequence from 30 to 200 K, while dotted lines are the same for modified blackbodies (optically thin dust having additional multiplicative factors of λ^{-1} and λ^{-2}, which may be important depending on grain size relative to wavelength). Although most objects are within 1–2 σ of the expected blackbody relationship, the systematic offset suggests that such single-temperature blackbody models may not be the most appropriate models. [*See the electronic edition of the Journal for a color version of this figure.*]

Detailed discussion of the source HD 107146 can clarify the logic. Using the 1 σ extremes on the photometry, the 24 μm/33 μm color temperature is nominally 72 K but could be in the range 64–81 K (72^{+9}_{-8} K), while the 33 μm/70 μm color temperature, nominally 52 K, could be in the range 50–54 K (52^{+2}_{-2} K). Those two temperature ranges are inconsistent at the >2 σ level. Fitting the 24 μm/33 μm color excess with the nominal color temperature that goes exactly through the data points requires a solid angle of dust $\Omega = 2.62 \times 10^{-14}$ sr; this model then predicts a 70 μm flux density 10 σ below the observed data. If, instead, we fit the 33 μm/70 μm color excess with the nominal color temperature, we require $\Omega = 2.87 \times 10^{-13}$ sr or 11 times larger solid angle than for the hot dust source; this model predicts a 24 μm excess that is low by 3.6 σ. As a compromise one could consider an intermediate temperature set by fitting the 24 μm/70 μm excess with a 58.5 K blackbody. To also fit the intermediate 33 μm point then requires a source size $\Omega = 1.09 \times 10^{-13}$ and leads to underpredictions at both 24 μm (by 2.6 σ) and 70 μm (by 5.7 σ). For several other stars the 24 μm excess amplitude is higher than it is for this star, and the required color temperatures are even farther apart.

One could postulate under the blackbody assumption that the range of temperatures inferred for our debris disks is caused by either a range in grain locations or a range in grain sizes. These location and/or size distributions may be distinct or continuous. In either scenario, if the different temperatures emanate from different components, with only a few flux density points measured in the excess, we cannot determine grain location or size as well as the temperature. A continuum of temperatures, indicating in the simple blackbody assumption material over a continuous set of distances from the star (aka a disk) or having a continuous distribution of sizes, encompasses the case of two or more distinct temperature components and so we adopt this more general model in what follows.

The grain size scenario, in which a range of small grain sizes from the blowout size upward maintain different temperatures at the same physical distance from the star (due to the different absorption/radiation efficiencies), would result in the observed photometry reflecting a weighted mean of the emission. For dust sizes 1–10 μm, a temperature dependency $T \propto a^{-1/5}$ (see footnote 13 in § 4.1.2), or even allowing for something as strong as $T \propto a^{-1/2}$ from the grain absorption/emission efficiencies, implies a factor of ~1.5–3 range in temperature. In an idealized size distribution such as $n(a) \propto a^{-3.5}$, the smaller 1 μm grains absorb ~3 times more starlight than the 10 μm grains. These smaller grains will then dominate the (nonblackbody) emission but will have only ~$\frac{1}{3}$ of their luminosity coming out in the longer wavelength tail we observe, which is emitted primarily by the larger cooler grains. Thus, we consider more worthy of exploration the radial range scenario, in which there are multiple grain locations leading to the temperature ranges. In support of this interpretation, the evidence from debris disks detected in scattered light seems to be that multiple rings or extended structures indeed are present (e.g., Stapelfeldt et al. 2004), which is an existence theorem only that may or may not apply to our particular debris disks (although it does apply to at least two of them; see § 5.1).

To model radially extended disks for the 12 candidate multi-temperature systems, we consider excesses in a photometric band as significant if they are >3 σ, or if they are only >2 σ when the excess in an adjacent band is >3 σ and the inferred color temperatures are decreasing with increasing wavelength. We assume blackbody grains and a flat surface density distribution with radius, $\Sigma(r) = \Sigma_0 r^\alpha$ with $\alpha = 0$. Although $\alpha = 0$ is thought most appropriate to radiation-dominated disks and $\alpha = -1$ or -1.5 perhaps more descriptive of collisionally dominated disks, the radial optical depth per logarithmic interval of r goes as α, so it is the dust at the inner radius that is responsible for most of the absorption and reemission. Results for lower α thus should be close to those for the uniform temperature ring. Further, Thébault & Augereau (2007, their Fig. 10) show specifically for a model $\alpha = -1.5$ initial distribution undergoing collisional evolution that the micron to submillimeter grains quickly establish a flat density distribution, and it is only the larger bodies that retain the steeper distribution.

With the surface density exponent fixed, we step through a grid of $R_{\rm inner}$ and $R_{\rm outer}$, calculating under the blackbody assumption the fractional surface density σ_o (a dimensionless quantity) at the disk inner edge that exactly matches the 70 μm excess flux density. We then find the combination of the above three parameters that produces the lowest residuals when fitted to the overall SED of the excess, letting the 70 μm point be fitted freely in this second stage. Our disk models certainly are nonunique, but they do allow estimates of disk parameters; $R_{\rm inner}$ can be constrained (minimum value) from the warm color excess, while $R_{\rm outer}$ can be constrained (minimum value) by finding the smallest radius that satisfies the ($F_{70\ \mu{\rm m}}$ − error) or ($F_{160\ \mu{\rm m}}$ − error) constraints. We present our extended disk modeling results in Table 6. We list lower limits to the range of radii inferred from these (blackbody) temperature estimates and refer the reader to § 4.1.2 for the caveats in interpreting these radii as physical constraints on the true location of the dust. Taken at face value, the values imply fractional disk widths $\delta R/R \approx (R_{\rm outer} - R_{\rm inner})/(R_{\rm outer} + R_{\rm inner})/2$ of at least factors of several. We emphasize that we are unable to constrain

the dust outer radii very well as the sensitivity and wavelength coverage of our observations does not fully probe the coolest dust. However, we are quite confident in our general result of extended disks.

Returning to HD 107146, our results derived to match the overall SED indicate dust from 14 to at least 200 AU for $\alpha = 0$ (or 12–92 AU for $\alpha = -0.5$). One could truncate the $\alpha = 0$ disk at 130 AU to undershoot the 70 μm flux density by 1 σ. For comparison, the single-temperature model for this system predicts dust at 15.5 AU for the 72 K grain temperature and 30 AU for the 52 K grain temperature.

As an illustration of the limited application of our approach, we call attention to the case of HD 141943. Fitting the 24 μm/33 μm color excess results in a nominal color temperature of 90 K, while fitting the 33 μm/70 μm color excess gives 81 K. Both temperatures produce an equally good fit to the overall SED (Table 4), and the hotter temperature leads to a derived inner disk radius of 15.7 AU, while the cooler temperature gives 19.3 AU. An extended disk model, which is fitted for illustration rather than because of poor χ^2_ν from the single-temperature fit, spans ~9–40 AU (Table 6) with better χ^2_ν but also more free parameters in the model.[17] An independently fitted disk model using the more sophisticated methods referred to in § 4.3 also produces an extended structure, from 9.5 to 42 AU and having $\Sigma_o(R_{\rm inner}) \approx 2 \times 10^{-5}$ g cm^{-2}, impressively close to the simple model although with the 1 σ confidence contour exceeding 50% of the nominal best-fit values. Conversely, the only other source with similarly consistent single-temperature blackbody fits to the 24 μm/33 μm and 33 μm/70 μm color temperatures is HD 209253, with derived temperatures of 77 and 70 K; a disk model fit to this source spans only 18.6–18.8 AU.

As evidenced from the χ^2_ν results, small differences in color temperature with wavelength are probably consistent within the 2–3 σ errors. For the majority of sources not presented in Table 6, extended disk fits lead, as for HD 209253 mentioned above, to <1 AU wide rings; exceptions are HD 145229 and HD 201219, to which >10 AU wide disks can be fitted (albeit with lower significance than for the sources in Table 6). We note that choosing a surface density exponent α other than zero, either positive (e.g., a disk having low-density warm and high-density cold components) or negative (e.g., a disk having highest density at its inner edge), would lead to an increase in the number of disks with inferred broad radial ranges. For example, a large negative value of α would place most of the particles (i.e., mass) near the inner edge of the disk and the SED would resemble a single-temperature/narrow ring model. In summary, we interpret the larger, most significant color temperature differences with wavelength as the most compelling SED evidence for extended disks.

4.3. *Potential for More Detailed Modeling*

In most cases, our 70 μm excess sources exhibit only a limited number of photometry points (sometimes just one) in excess, and simple blackbody models, either with or without geometric complexity, are sufficient. More detailed modeling may be warranted in several cases, however. Candidates include HD 8907 (e.g., Kim et al. 2005), HD 104860, and HD 107146, which have multi-wavelength submillimeter photometry (see Fig. 8), and HD 61005 and HD 107146 (again), which are both spatially resolved in scattered light at optical/infrared wavelengths (HD 107146 is resolved as well at submillimeter/millimeter wavelengths, measuring thermal emission). We can use any such results to inform our strong assumptions made above in deriving values of dust temperature, location, luminosity, and mass.

As an example of what is possible, HD 38529 has been analyzed in some detail by Moro-Martín et al. (2007). This source is of particular interest due to the presence of multiple planets detected via the radial velocity method. The characteristic dust temperature derived here from the ratio of 33 μm to 70 μm excess emission is <48 K, implying dust at >98 AU in the blackbody assumption (see Table 5). The temperature derived from fitting a photosphere plus a single-temperature blackbody to the shorter wavelength IRS spectrum is 79 K, implying dust at 31 AU assuming blackbody emission (J. M. Carpenter et al. 2008a, in preparation). As with the sources in § 4.2, this difference in HD 38529 dust temperatures derived for different wavelength ranges indicates that the dust probably is not confined to a narrow ring. Moro-Martín et al. (2007) explored the complexity and degeneracy of debris disk SED modeling in the nonblackbody grain case using the radiative transfer code developed by Wolf & Hillenbrand (2003). They found for 10 μm astronomical silicate grains in a dust annulus having free parameters $R_{\rm inner}$, $R_{\rm outer}$, $M_{\rm dust}$, and Σ_0 (initially assumed constant with radius) that the derived $R_{\rm inner}$ increases (1) as $R_{\rm outer}$ decreases, because for a given dust mass, smaller $R_{\rm outer}$ means a larger Σ_0, and hence more warm dust needs to be eliminated in order to be consistent with lack of 24 μm–emitting dust in this particular source; (2) as Σ becomes steeper (e.g., $\Sigma \propto r^{-1}$ instead of constant); and (3) as smaller grains are considered. Because the outer radius of the disk, $R_{\rm outer}$, cannot be constrained with data currently available, it was found that a wide range of overall disk properties (dust location, total mass, and luminosity) are consistent with the sparsely sampled SED.

Similar modeling of the other sources presented in this paper would have comparably uncertain results, and we do not attempt it here. However, in the case of HD 38529, one can move beyond SED degeneracies by using dynamical simulations that take into account the role of mean motion and secular resonances of the two known planetary companions, to study the location of stable niches of potential dust-producing planetesimals. Moro-Martin et al. (2007) concluded from such dynamical modeling that the planetesimals responsible for most of the dust emission are likely located within the 20–50 AU region, one of the possible results from the SED modeling and consistent with the ~100 AU inner dust edge in the simple blackbody scenario adopted here. Similar procedures may become possible for other FEPS targets if the planetary systems are discovered directly.

4.4. *Inner Cleared Regions*

Neither the spatially resolved imaging of inner disk holes nor the detection of planets that would enable inference of inner clearings based on dynamical analysis is available yet for most of our sources. However, our simple modeling procedure has led to the result that the dust excess is dominated by a cold component that contributes prominently to the SED at 70 μm and is typically located exterior to ~10 AU. P-R radiation drag causes dust at large radii to spiral in toward the central star on timescales of only millions of years. Even in collisionally dominated disks such as we think dominate our sample (§ 5.3), some grains will avoid collisions and migrate to the inner disk.

We can ask the question of whether the inferred values of $R_{\rm inner}$ imply a lack of substantial amounts of warmer dust closer to the star, by testing how much mass could be hidden interior to $R_{\rm inner}$ without producing detectable radiation at the shorter

[17] The reason an extended disk model leads to a smaller inner radius than the single-temperature blackbody matched to the 24 μm/33 μm color excess is because the former is a fit to the broader SED including errors, rather than a calculation specific to the exact 24 μm/33 μm flux ratio.

Spitzer wavelengths. To do so, we adopt the same 10 μm average grain size as above, such that the opacity scales only with surface density. We also assume the flat surface density profile [$\Sigma(r) = \Sigma_0 r^0$] appropriate for the radiation-dominated, relatively cleared inner region that we postulate could extend from $R_{\rm inner}$ to an R_0 that corresponds to the dust sublimation temperature at 1500 K. We then find the corresponding dust mass such that the most stringently confining flux density not observed in excess among the 13, 24, and 33 μm measurements is not violated by more than 1 σ; we note that it is usually the 24 μm point that provides the best limit.

The resulting dust masses are small, roughly 10^{-6} to $10^{-4}\,M_\oplus$, and would decrease if we decreased the assumed grain size (§ 4.1). This corresponds to roughly a single asteroid mass pulverized into micron-sized grains. The surface density contrast between any such low-mass inner dust disk and the outer dust disk that we in fact observe can be constrained by fitting a two-component model with surface density $\Sigma_{o,\rm inner}(r/r_{o,\rm inner})^0$ in the hypothetical inner P-R–dominated disk and $\Sigma_{o,\rm outer}(r/r_{o,\rm outer})^{-1\ \rm or\ 0}$ in the outer collision-dominated disk (recall the Thébault & Augereau [2007] result noted earlier regarding the quick establishment of a flat surface density profile for the dust—even in a collisionally dominated disk). Resulting values of $\Sigma_{0,\rm outer}/\Sigma_{0,\rm inner}$ range from >30 at the minimum to $\gg 10^5$ depending on model choices. For example, if we assume a very large (200 AU) outer disk, it requires relatively little surface density to match the 70 μm measurement, compared to a narrower disk or belt that would require substantially more (factor of $\sim 10^3$) surface density and hence produce larger outer/inner disk contrast than the minimum quoted above. Similarly, a declining surface density profile for the outer disk also requires more (factor of $\sim 10^2$) surface density relative to the flat surface density profile and hence would also enhance the above minimum contrast numbers.

5. PHYSICAL IMPLICATIONS

5.1. *Extended Dust Disks*

Tables 5 and 6 show the characteristic location of the dust for single-temperature blackbody models and for extended disk models, respectively. Of note is that for a number of systems with high $L_{\rm dust}/L_*$, we have inferred the existence of dust disks of wide radial extent.

The best evidence for extended disks around other dusty stars has come from spatially resolved imaging in both scattered light at short wavelengths and thermal emission at longer wavelengths. Prominent nearby examples of non–narrow ring sources include the very young (10–20 Myr) debris disks AU Mic (M-type star) and β Pic (A-type star), as well as the somewhat older systems ϵ Eri and HD 53143 (K-type stars), HD 32297 (G-type star), and Vega and 49 Ceti (A-type stars). The spatially resolved images indicate dust over a wide range of radii. In most cases the data are contrast limited at the inner edges, implying widths >50 AU (Ardila et al. 2004; Kalas et al. 2006), roughly consistent with our understanding of the solar system's dust distribution having width 25–30 AU beginning outside 30 AU. From the SEDs, alone, one would not have inferred the presence of multitemperature material for these particular sources. Indeed, it is rare to infer extended debris dust from SEDs.

There are two FEPS sources, both in our 70 μm excess sample, that have been spatially resolved. HD 107146 (first discussed as an infrared excess object by Metchev et al. 2004; Williams et al. 2004) is the first spatially resolved disk associated with a G-type star (Ardila et al. 2004; Carpenter et al. 2005; Metchev et al. 2008) and extends from 80 to 185 AU optically and from 30 to 150 AU at submillimeter wavelengths. HD 61005 (first discussed as an excess object here) is spatially resolved in scattered light (Hines et al. 2007). Both objects also appear in our Table 6 of candidate extended disks. That we infer extended dust geometries based on SEDs for several additional FEPS sources indicates that they are prime targets for high spatial resolution, high-contrast observations that might succeed in imaging the disks.

5.2. *Steady State versus Stochastic Collisions*

The debris disk systems discussed here have dust at temperatures and locations roughly comparable to the inner regions of the solar system's own Kuiper Belt. However, the $f = L_{\rm dust}/L_*$ values that result from our simple blackbody modeling indicate much higher levels of dust: $L_{\rm dust}/L_* \sim 10^{-4.5}$ to $\sim 10^{-3}$ compared to the $\sim 10^{-7}$ to 10^{-6} inferred for the Kuiper Belt (Fixsen & Dwek 2002; Backman et al. 1995; Stern 1996a). Higher values of $L_{\rm dust}/L_*$ at the same location suggest that our disks contain more dust than our present-day solar system.

By experimental design, the FEPS sources typically are younger than our solar system (only 6/328 are comparably aged or older according to our most recent age estimates). A more appropriate comparison of the dust luminosities and masses might be made, therefore, to models of the earlier dust content in the solar system. Because the relevant processes are dissipative, we cannot extrapolate backward in time. However, we can use forward modeling that assumes τ^{-1} (for a collision-dominated dust disk) or τ^{-2} (for a radiation-dominated dust disk) scaling as may be appropriate during different stages of solar system dust evolution (e.g., Dominik & Decin 2003). See § 3.1 and Meyer et al. (2007) for brief discussion of such a model. Our data would thus be explained in the context of our solar system by a more massive planetesimal belt(s) (e.g., Wyatt 2006).

Alternate to the more massive and perhaps younger debris disk scenario, we could be witnessing the effects of transient phases of high dust production due to recent massive collisional events in these particular 70 μm–bright systems (e.g., Jura 2004). If all the observed disks were transient, our observations could be used to assess the duty cycle of such short-lived events given the rapid blowout times for small grains, once produced. If, for example, we are detecting 10% of systems in states that should disperse in 1% of the system lifetimes, and assuming that all stars go through this process, then we would be seeing a phenomenon that occurs 10 times in the lifetime of the system, rather than single, unique catastrophes.

To assess whether the observed dust could be produced by the steady grinding down of planetesimals or, on the contrary, if a transient event is required, we can compare the observed excess ratio, f, to that corresponding to the maximum dust production rate that could be sustained for the age of the system, an $f_{\rm max}$. Following Wyatt et al. (2007) and using the same parameters for debris belt width (50%), planetesimal strength, maximum planetesimal size, and orbital parameters, we find that

$$f_{\rm max} = 0.00016\left(\frac{R}{\rm AU}\right)^{7/3}\left(\frac{\tau}{\rm Myr}\right)^{-1}\left(\frac{M_*}{M_\odot}\right)^{-5/6}\left(\frac{L_*}{L_\odot}\right)^{-0.5}.$$

This equation represents equilibrium evolution of a standard $a^{-3.5}$ grain size distribution with no grain growth or planetesimal accretion. Most of the FEPS 70 μm–selected debris disks appear below the predicted line, by up to 2 orders of magnitude, although some are very close to it. Exceptions for which $f > f_{\rm max}$ are HD 206374 and HD 85301. The former is a marginal excess detection. The latter is a factor of a few above the collisional prediction [which is

notably the lowest f_{max} among our sample stars] and could therefore be a rare stochastic system. With $f < f_{max}$ in general, the FEPS debris disks appear consistent with a steady grinding down of planetesimals. This is also the conclusion reached by Löhne et al. (2008), who find, unlike Wyatt et al. (2007), a dependence of f on initial disk mass and an evolutionary behavior of f with shallower slope ($\tau^{-0.3}$ rather than τ^{-1}).

Another comparison that can be made is to the planetesimal formation and early debris "self-stirring" models of Kenyon & Bromley (2005), which predict a peak in f between 10 and 100 Myr, rather than the monotonic steady decay of Dominik & Decin (2003), Wyatt et al. (2007), or Löhne et al. (2008). The FEPS data may be more consistent with this genre of collisional evolution at the young ages; see J. M. Carpenter et al. (2008a, in preparation) for in-depth comparison to these particular models and discussion of the evolution of debris having a range of temperatures and locations (regardless of detectability at 70 μm). That our highest f-values occur roughly around 100 Myr (§ 6.1) may also be indicative of consistency with these models.

In summary, we find no strong evidence for transiently bright dust among our sample of 70 μm–selected disks. Rather, our brightest 70 μm–selected debris systems seem consistent with massive, youthful debris disks undergoing collisional evolution.

5.3. *Radiation-dominated versus Collision-dominated Disks*

To further evaluate the possibilities regarding the steady state evolution versus stochastic event interpretation of debris around solar-type stars, we address in this section whether our detected debris disks are collision dominated or radiation dominated. We consider the timescales for various processes (following Backman & Paresce 1993) and then evaluate their relation and appropriateness to our debris disks:

Collisional lifetime.—The time between collisions involving a single grain can be estimated simply as $1/n\sigma v$. Under the presumptions of circular orbits and completely destructive collisions between grains of the same size, this becomes

$$\frac{\tau_{\rm collisions}}{\rm yr} > \left(\frac{R}{\rm AU}\right)^{1.5} \frac{1}{9\sigma(R)\sqrt{M_*/M_\odot}},$$

where $\sigma(R)$ is the face-on fractional surface density, in units of cm^2 of grain cross section per cm^2 of disk area, also termed radial optical depth (see below). For a constant surface density, $\Sigma(r) \propto r^0$, $\sigma(R) = 2f/\ln(R_{\rm outer}/R_{\rm inner})$, with $R_{\rm inner}$ the inner disk boundary and $R_{\rm outer}$ the outer disk radius (e.g., Backman 2004). Then in the case of a broad belt with $R_{\rm outer}/R_{\rm inner} \sim 7$, $\ln(R_{\rm outer}/R_{\rm inner}) = 2$ and $\sigma(R)$ is simply $\approx f = L_{\rm dust}/L_*$. Thébault & Augereau (2007) propose a significant modification to the above formula that accounts for the grain size distribution as a scaling factor of $[(a/1.2a_{\rm min})^{-2} + (a/100a_{\rm min})^{2/7}]$; this lengthens the collision lifetime by up to a factor of 10 for grains very near the blowout size and shortens it by up to a factor of 100 for grains less than 100 times the blowout size (maximally so for grains $\sim$10 times blowout size), and again lengthens the collision lifetime for even larger grains. Because we generally consider grains of several times the blowout size, we note that from the simple formula above the derived collision times are likely overestimates, i.e., the true collision timescales for average grains in our disks are even shorter than the values we calculate, roughly 10^4–$10^{5.5}$ yr.

Radiative blowout lifetime.—For very small grains, the relevant timescale is the travel time for removal from the disk under the influence of radiation pressure. This occurs when the radiative force exceeds the gravitational force. The time it takes for a grain to go from $R_{\rm inner}$ to, say, $4R_{\rm inner}$, where, under the blackbody assumption, the grain temperature is reduced by half so that the grain no longer contributes significantly to the flux density measured at $R_{\rm inner}$, is given by

$$\frac{\tau_{\rm blowout}}{\rm yr} = 0.5\sqrt{\frac{(R/{\rm AU})^3}{(M_*/M_\odot)}}.$$

The so-called blowout time is generally many orders of magnitude smaller than the other timescales, roughly 10^1–$10^{2.5}$ yr.

P-R lifetime.—For grains larger than the blowout size (formula given in § 4.1.3), the time it takes for a dust grain to spiral inward under the effect of P-R drag from a distance R all the way to the star ($R \approx 0$) is given by

$$\frac{\tau_{\rm P\text{-}R}}{\rm yr} = 720\,\frac{(\rho/{\rm g\ cm^3})(a/\mu{\rm m})(R/{\rm AU})^2}{(L_*/L_\odot)(1+{\rm albedo})}.$$

To estimate the time it would take for a grain to drift from a distance R_2 to a distance R_1, we substitute R^2 by $(R_2^2 - R_1^2)$. Replacing R^2 by $(R_{\rm outer}^2 - R_{\rm inner}^2)$ gives the timescale for a particle to move through the entire debris belt, which can be compared to the time for particles in the belt to collide, as given above. For our disks we calculate radiative drift times ranging from $10^{5.5}$ to $10^{7.5}$ yr.

Corpuscular drag lifetime.—The effect of stellar wind (or corpuscular) drag scales with the P-R lifetime as

$$\tau_{\rm wind} = \frac{L_*}{\dot{M}_{\rm wind}c^2}\,\tau_{\rm P\text{-}R},$$

assuming comparable coupling efficiencies or Q-values for wind and P-R drag (Jura 2004). While less important for relatively old stars like the Sun, for which $\dot{M}_{\rm wind} = 3\times10^{-14}\ M_\odot\ {\rm yr}^{-1}$ and hence $\tau_{\rm wind} \approx 3\tau_{\rm P\text{-}R}$, wind drag may be relevant for young stars such as FEPS targets, which may have much higher mass-loss rates at the same or only slightly higher stellar luminosity L_*. There is still significant uncertainty in the appropriate values, however (e.g., Wood et al. 2005; Matt & Pudritz 2007), and so we do not consider further the details of this potentially relevant dust removal mechanism.

At issue is whether the dust grains we observe will disappear by moving outward from the planetesimal belt (which would be the case in collision-dominated systems where dust particles erode and fragments blow out), or whether they spiral inward toward the star producing a zodiacal-like dust cloud located between the inner edge of the planetesimal belt ($R_{\rm inner}$) and the star (like would happen in a P-R–dominated system such as the inner solar system). As the processes are statistical in nature, the question can be partially addressed by comparing the collisional lifetime to the time it takes a grain to migrate. In the above equations, when the surface density profile exponent $\alpha = 0$, $\tau_{\rm collisional}$ increases as $r^{1.5}$ and $\tau_{\rm P\text{-}R}$ increases as r^2; thus, if $\tau_{\rm collisional} \ll \tau_{\rm P\text{-}R}$ at $R = R_{\rm inner}$, then this condition will hold throughout the disk, at all points $R > R_{\rm inner}$. In an $\alpha = -1$ disk, $\tau_{\rm collisional}$ increases as $r^{2.5}$, and if as above $\tau_{\rm P\text{-}R} \gg \tau_{\rm collisional}$, but now at $R_{\rm outer}$, then this condition will hold toward the inner disk, at all points $R < R_{\rm outer}$. In what follows we demonstrate that the disks are collisionally dominated at $R_{\rm inner}$ (and therefore throughout, if $\alpha = 0$), as well as at an assumed $R_{\rm outer}$ (and therefore throughout, if $\alpha = -1$).

We can consider migration between a characteristic point in the middle of the belt ($R_{\rm mid}$) and either $R_{\rm inner}$ or $R_{\rm outer}$. Those

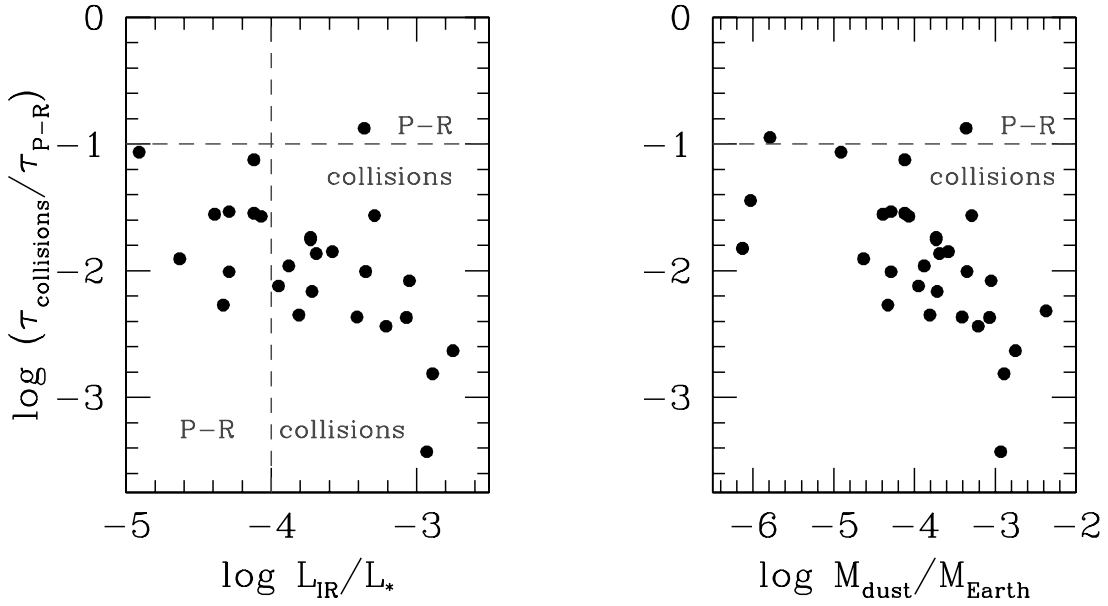

FIG. 11.—Correlation of the timescales for collisional vs. radiative processes in the disks, with measured fractional dust luminosity $f = L_{dust}/L_*$ and inferred dust mass $M_{dust,\,min}/M_\oplus$. Divisions between radiation-dominated and collision-dominated regimes (Wyatt 2005) are shown as dashed lines, for rough guidance only. The timescales are calculated relative to the inner radius for an $\alpha = 0$ surface density profile; using the outer radius and $\alpha = -1$ increases the timescale ratio by about an order of magnitude. [*See the electronic edition of the Journal for a color version of this figure.*]

reaching R_{outer} from the interior are lost from the system, and it is assumed that all grains small enough to undergo blowout are thus quickly removed. Those reaching R_{inner} from original locations between R_{mid} and R_{inner} would create a zodiacal cloud and be able to drift past R_{inner} before colliding. A reasonable value for R_{mid} is $\sqrt{2}R_{inner}$, and in this case the P-R drift timescale is numerically equal to the P-R lifetime derived above for $R = R_{inner}$. Alternately, Moro-Martín et al. (2007) calculate the time it takes grains to fill the inner gap as $\tau_{fill} = [1 - (1 - x/100)^2]\tau_{P\text{-}R}$, where x is a percentage scaling (assumed to be 10%) of R_{inner} over which the dust density decreases.

The disk optical depth is roughly f, with vertical optical depth $\approx\frac{1}{3}$ radial optical depth, that in the disk plane, which above was called the dimensionless face-on surface density (see also Backman 2004). For small values of the fractional infrared luminosity (i.e., optical depth) $f = L_{dust}/L_* < 10^{-4}$, the primary effects on the dust population are radiative (e.g., P-R drag and blowout) and/or mechanical (e.g., stellar wind). When dust removal is dominated by these mechanisms, the radial distribution of the existing dust is expected to extend over a larger radial range than the location of the parent bodies generating the dust (such as may be the case for Vega [Su et al. 2005] and ϵ Eri [D. Backman et al. 2008, in preparation]). Conversely, for large values of $L_{dust}/L_* > 10^{-4}$, such as we report here, the disks are expected to be collisionally dominated (e.g., Krivov et al. 2000) with larger grains cascading into smaller grains on timescales shorter than they are affected by the above-mentioned grain removal processes. In this case, the radial distribution of the dust is expected to mimic that of the parent bodies colliding to produce the dust, and to undergo further collisions in situ.

In Figure 11 we compare the collisional and radiative removal timescales with both the L_{dust}/L_* and M_{dust} values. In Table 5 we consider both situations described above: the $\alpha = 0$ disk evaluated at the $R = R_{inner}$ inferred from the assumed blackbody scenario, and the $\alpha = -1$ disk evaluated at an $R = R_{outer}$, which is unconstrained by the observations but assumed to be 200 AU for purposes of illustration. In the former case, $\tau_{collisions}/\tau_{P\text{-}R} \propto 1/\sqrt{R}$ and so the 10%–30% uncertainties in R_{inner} are not a large effect. Our calculations consider only a single grain size, 10 μm, with $\tau_{collisions}/\tau_{P\text{-}R} \propto 1/\sqrt{a}$ (Wyatt 2005). We conclude that for the debris disks discussed in this paper, the observed fractional infrared luminosities, $L_{dust}/L_* \gtrsim 10^{-4}$, imply $\tau_{collisions}/\tau_{P\text{-}R}$ in the range 10^{-3} to 10^{-1} near the inner edge of the disk; i.e., the dynamics of the dust particles in these disks is indeed dominated by collisions. Similar analysis by Dominik & Decin (2003) and Wyatt (2005) of previously known bright debris disks has led to similar conclusions: that they are all collision dominated. Even for our evaluation at a fabricated outer disk radius of 200 AU and a falling surface density profile, the values of $\tau_{collisions}/\tau_{P\text{-}R}$ are an order of magnitude higher than at R_{inner} and a flat surface density profile, but generally less than unity; a few cases have ratios higher than unity by factors of several. Among our sample, HD 38529 stands out with the highest ratio of $\tau_{collisions}/\tau_{P\text{-}R}$ (in either scenario), suggesting a long collision timescale likely because of the large inner radius of the disk; hence, P-R effects may play a more prominent role for this particular system relative to the others.

Although the small grains produced in collisionally dominated disks are blown out by radiation pressure, grains larger than the blowout size cascade into smaller grains before they have time to migrate far from the dust-producing planetesimals under the effect of P-R drag. Even in collisionally dominated disks in which each collision preserves, say, roughly $1/e$ of the grains, some small percentage (5% of grains survive three collisions while $\sim$1% of grains survive five collisions) of the dust particles may survive long enough to have a chance to undergo P-R drag and thus permeate the inner disk. The debris disks around 49 Ceti (Wahhaj et al. 2007) and ϵ Eri (D. Backman et al. 2008, in preparation), with small grains in the inner disk contributing to spatially resolved mid-infrared emission and little to the SED, but large grains in the outer disk contributing most of the excess in the SED, may be examples of exactly this phenomenon. In § 4.4 we reported $<10^{-6}$ to 10^{-4} $M_\oplus$ in dust within the inner cleared regions of our debris systems.

5.4. *Location of the Dust-producing Planetesimals and Potential Planets*

We concluded above from examination of the timescales involved in different dust production and dust removal mechanisms that the disks we observe are collisional. Hence, the dust and the parent bodies are expected to be colocated.

We consider now as a general question whether the wide radial extent inferred for the dust implies a similarly wide planetesimal belt. When dust particles are released from their parent planetesimals, their semimajor axes increase due to the effect of radiation pressure, instantaneously from r to $r' = r[(1 - \beta)/(1 - 2\beta r/r_{\rm rel})]$ (Burns 1979), where β is the dimensionless ratio between radiation pressure force and gravitational force and $r_{\rm rel}$ is the radius of the dust release point. For $\sim$10 μm silicate grains with optical constants from Weingartner & Draine (2001) and assuming $\beta \sim 0.025$ as in the solar system, $r' = 1.026r$. Other combinations of larger β-values (0.05, 0.2, and 0.4), which imply smaller grains for the same radiation field (4.5, 1.3, and 0.7 μm, respectively), lead to $r' = 1.05r$, $1.3r$, and $3r$. The increase in semimajor axis is therefore small for the big grains that we expect dominate the 70 μm emission but can be large as the blowout size is approached, consistent with intuition. Assuming the large grain case, if the planetesimals were located in just a narrow ring, they therefore cannot account for the large difference found between $R_{\rm inner}$ and $R_{\rm outer}$ in the dust modeling. This suggests that our disks likely harbor wide planetesimal belts roughly comparable in size to their wide dust belts.

Separately, the strong depletion of warm dust, inferred from lack of short-wavelength excess emission, also has implications if it can be argued that the inner edge of the dust distribution betrays an inner edge to the planetesimal distribution. Possible processes that would create such inner edges are the presence at early times of large (1000 km) planetesimals that could have stirred up and ground away the inner region of the planetesimal disk, or the existence today of gravitational perturbations due to one or more planetary companions on the planetesimals, as argued for HD 38529 by Moro-Martín et al. (2007).

For radiation-dominated disks, an inner cleared disk geometry is often used to suggest the presence of a planet that is sufficiently massive to not only stir the exterior planetesimals, increasing their velocity dispersion such that dust-producing collisions occur, but also then either eject efficiently any dust particles that cross its orbit as they spiral in due to P-R drag (>80% of the particles are ejected by a 1–10 M_J planet in a circular orbit at 1–30 AU; Moro-Martín & Malhotra 2002, 2003, 2005) or/and trap them into temporary resonances as they migrate inward (e.g., Ozernoy et al. 2000). Such scenarios prevent or at least impede material from reaching radii much smaller than those where the dust is in fact detected.

For collision-dominated disks, such as we infer here, the location of the planetesimal-stirring planets is less obvious and requires detailed modeling of individual systems once they can be spatially resolved.

6. COOL DUST TRENDS WITH STELLAR PARAMETERS

Overall, FEPS finds 37/328 stars with 70 μm excess. Six of these are young primordial disks with excess emission extending from <8 μm to >70 μm. Removing these six results in an overall incidence of 70 μm excess indicative of cool debris, of 10% within FEPS. Further accounting for the fact that 14 of the FEPS sources were chosen for the program based on previous suspicion of having infrared excess (only 12 of which are confirmed as such) yields a 6% excess fraction at 70 μm. We consider these percentages lower limits due to the sensitivity-limited observations.

The majority of the 70 μm excess sources also have 33 μm excess and/or 24 μm excess indicating that the dust is within 5–30 AU. Meyer et al. (2008) and J. M. Carpenter et al. (2008a, in preparation) present a more complete picture of excess versus wavelength and versus age/mass. In Figure 12 we present detected and 3 σ upper limits to fractional excess luminosities based on our 70 μm data analysis, compared to both stellar age and stellar temperature/luminosity. The f-values are determined as above for the 70 μm detections and as 3 σ maxima to (the minimum) f for the 70 μm upper limits assuming a hypothetical dust SED that peaks at 70 μm (using the formula in § 4.1.2). Note that these values could be factors of several higher for hotter dust or orders of magnitude higher for cooler dust not peaking at 70 μm (see Fig. 9). Note also that these values are still upper limits because the flux densities are upper limits.

6.1. *Stellar Age*

The primary goal of the FEPS Legacy survey is to trace the time evolution of dusty debris around solar-type stars. Proper assessment requires consideration of the full SED. This would allow physical parameters such as $T_{\rm dust}$ and $R_{\rm dust}$ to drive the discussion rather than empirical or wavelength-driven constraints, such as are imposed here. However, mindful of the observational biases that render the great majority of FEPS 70 μm observations upper limits and the 70 μm detections almost all excess objects, we summarize a first analysis of cold debris disk evolution with age. Stellar age determinations for the FEPS sample are discussed in detail by L. A. Hillenbrand et al. (2008, in preparation). In brief, a variety of age indicators such as coronal activity, chromospheric activity, stellar rotation, lithium abundance, and the Hertzsprung-Russell diagram are calibrated to open clusters and used to assess stellar ages between 3 Myr and 3 Gyr. Rough ages for the sample of 70 μm excess sources are provided in Table 1.

In Figure 12, there is no apparent trend in 70 μm dust detection frequency with stellar age, other than a dearth of strong debris-type excesses in our youngest age bins 3–10 Myr.[18] Further, comparison of the age distribution for the detected (using either 2 or 3 σ threshold) and the nondetected objects is insignificant using the K-S test, suggesting that we cannot distinguish them. The excess amplitude at 70 μm does, however, appear to decline with age, most obviously in the upper bound; this could be significant when coupled with an invariant excess frequency with age. Analysis of a more physical quantity like $L_{\rm dust}/L_*$, as illustrated, reveals that the average value and the upper bound (including measured as well as upper limits on $L_{\rm dust}/L_*$) decrease with age. Given the large scatter in $L_{\rm dust}/L_*$ values (both measured and upper limit) at all ages and the intermingling of detections and nondetections in f, we do not draw any strong conclusions regarding the physical implications of this trend.

Of interest is that the four highest values of f among our debris disk sample (HD 61005, HD 38207, HD 191089, and HD 101746) all occur within the narrow age range 80–200 Myr. Note that each of these high-f debris systems is suggested in Table 6 as a radially extended disk. There are no trends in either the evidence for an extended disk or the derived $\delta R/R$ values among the extended disks with stellar age. For the entire debris sample detected at 70 μm, there are no apparent trends in derived $T_{\rm dust}$, $R_{\rm dust}$, or $M_{\rm dust}$ with age. An outlier object in such scatter plots is HD 38529 with a very large inferred inner dust

[18] There are six *primordial* disk excesses in this age range, but the remainder of this young sample is undetected at 70 μm.

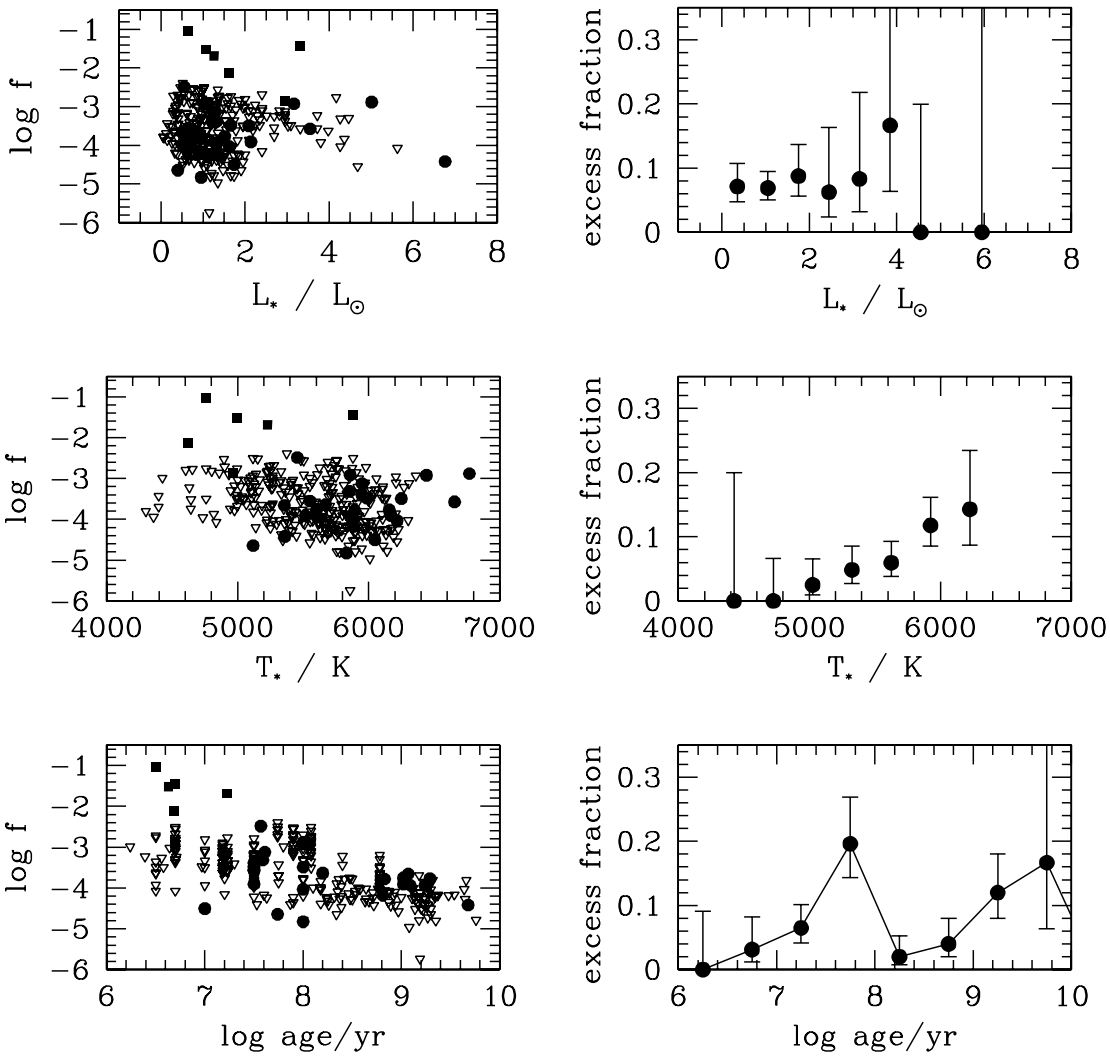

FIG. 12.—The 70 μm excess statistics as a function of stellar age (*bottom panels*) and stellar temperature and luminosity (*middle and top panels, respectively*). *Left*: Fractional excess luminosity due to dust ($f = L_{\rm dust}/L_*$); triangles are sources with no detected 70 um excess, plotted at 3 σ upper limits; filled circles are detected debris disks; and filled squares are detected primordial disks. *Right*: Frequency of excess detection. We suggest a correlation in the upper bound of f with stellar age, but no trends in f with stellar mass or luminosity. We do not find trends in the 70 μm dust detection frequency with stellar age or luminosity but do suggest that there may be a trend with stellar mass below 6400 K where the sample is unbiased. Note that there are two bins at high temperature and high luminosity that exceed the range of the plot along the ordinate.

radius, perhaps driven by its larger than average stellar luminosity or the presence of a sculpting planet.

6.2. *Stellar Mass*

In addition to the lack of $T_{\rm dust}$, $R_{\rm dust}$, or $M_{\rm dust}$ dependence with age among our detections, there are, similarly, no trends of these parameters (nor of f) with T_* or L_*. Note that because our sample spans a range of ages from ~3 Myr to 3 Gyr, there is not a 1 : 1 correlation between T_* and L_* as would be true for a purely main-sequence sample lacking young objects; thus, we show both in Figure 12. In contrast to the situation for stellar ages where we found a trend in f with age but no evidence for a trend in detection frequency with age, here for masses we do not find any correlation with f (or other parameters), but we do find a trend in the dust detection *frequency* at 70 μm.

Among our sample of 70 μm debris disks, 10 are F stars, 20 are G stars, and just two are K stars. The relative search samples in the total FEPS program are 42, 181, and 77 stars with spectral types F, G, and early K, corresponding to detection percentages of 24%, 10%, and 3%, respectively. Only three of the excess G stars are G5 and later, rendering the above percentages 24%, 12%, 7%, and 3% for F, G0–G4, G5–G8, and early K types, respectively. Finally, excluding those sources with 70 μm excesses that were known from previous work with *IRAS* and *ISO* (see Table 1) leaves 3/35 (9%) among F stars, 16/178 (9%) among G stars, and 1/76 (1%) among early K stars detected. The trend of less frequently detected debris dust around the later type stars is very clear when detection frequency is correlated directly with the inferred T_* (see Fig. 12), noting only the points below 6400 K where the sample is not biased by excess objects chosen for the probe of disk gas evolution. We emphasize that the trend is not driven by any trend in debris frequency with L_*, which is flat for the bulk of our sample even at fixed T_*.

These findings are consistent with the relative detection frequencies of debris among A star samples, FGK samples, and M star samples having a wide range of ages (e.g., Rieke et al. 2005; Meyer et al. 2008; Gautier et al. 2007). For example, Beichman et al. (2006) claim that they did not detect in their more limited survey any debris disks around 23 stars later than K1, "a result that is bolstered by a lack of excess around any of the 38 K1–M6 stars in two companion surveys." The FEPS sample shows similar behavior for stars typically younger than the Beichman sample. However, it is not yet clear whether all relevant variables, observational (including selection effects) as well as astrophysical,

have been normalized properly among the various samples, as would be required before such claims can be validated.

To assess the significance of the apparent trend reported here among our FGK sample, we consider again our lack of sensitivity at 70 μm to stellar photospheres. First, the distance range of the FEPS sample is peaked at $d < 50$ pc for all spectral types, with a long tail in the distance distribution out to 180 pc. The F star sample contains no objects at distances between 70 and 120 pc, but the 10 excess F stars include objects with both $d < 70$ pc and $d > 120$ pc. The G and K star samples cover the full distance range $\sim$10–180 pc with the two excess K stars both nearby (26 and 10 pc). We conclude that distance effects do not bias the apparent trend with spectral type. A second consideration is the relative age distributions. The K star sample peaks at younger age than the F and G samples, but there are similar numbers of F, G, and K stars at all ages older than 100 Myr. Thus, age effects (which we have not claimed for the sample as a whole) also do not seem to bias the results on debris versus stellar temperature/mass since, if anything, the younger K stars might be expected to have a higher incidence of detectable disks rather than a lower incidence.

A final consideration is whether we can reach the same value of $f = L_{\rm dust}/L_*$ for later type (generally less luminous and cooler) as for earlier type stars. A monochromatic debris detection trend with mass such as we report might be expected if it is driven by temperature or luminosity effects given that hot/luminous stars are capable of illuminating the same amount of dust to produce higher dust luminosity relative to cooler and less luminous stars in a flux-limited survey. There are no trends either in the limits or in the observed (detected) values of f, with either L_* or T_*. Again, we stress the several orders of magnitude spread in f and the intermingling of detections and upper limits over this range. It is only the *frequency* of detection that varies with the stellar temperature but not the luminosity. We conclude, although admittedly have not proven, that decreasing detection frequency toward cooler, less luminous, and typically less massive stars is not a result of varying sensitivity limits or luminosity effects. We believe that this again confirms our earlier assertion (recall discussion in §§ 3.1 and 3.2) that the dominant sensitivity limitation for FEPS 70 μm observations is primarily infrared background.

7. COMPARISON TO THE SOLAR SYSTEM AND CONTEXT RELATIVE TO OTHER WORK

We have identified 25 secure (tier 1) and six candidate (tier 2) debris disks in the FEPS sample. Considering their 33–70 μm color temperatures, approximately 25% of the systems have cold "Kuiper Belt–like" temperatures, $T < 50$ K, and $R > 30$ AU. Another 45% of the systems have "Jovian-like" temperatures, 60 K $< T <$ 120 K, and R in the range 5–20 AU. About 30% of the objects in our sample have characteristic temperatures 50–60 K, which would be analogous to "Uranus-Neptune zone" temperatures at 20–30 AU. Interestingly, there are no planetesimals in this region of the solar system, due to the earlier migration of the outer planets (in particular Neptune; e.g., Morbidelli et al. 2007). Only a small percentage (5%–10%) of our 70 μm–selected sources have evidence at shorter wavelengths for "asteroidal" belts with temperatures above 125 K, roughly corresponding to dust at $R < 5$ AU.

In $>\frac{1}{3}$ of the debris objects, disk models having broad temperature/radius ranges rather than single-temperature/radius models can be fitted. For these 12 objects (see Table 6) the data typically indicate material lying across more than a factor of 2–5 in radius.

The wide belts can be compared to the solar system's 2–4 AU asteroid belt having $\delta R/R = 2$ AU/3 AU = 66% or the 40–65 AU (estimated) Kuiper Belt with $\delta R/R = 25$ AU)/50 AU = 50%. These relatively narrow belts or rings in our solar system and elsewhere would be well described by a single-temperature blackbody model, in contrast to the subset of FEPS debris disks we propose as extended disk candidates. Assuming small grains instead of blackbody grains would move both the inner and the outer radii of the wide disks to larger values but would not change the fundamental result of disk breadth.

Although the dust temperatures and radii that we have derived from our debris disk modeling compare well to those characterizing the cold outer dust in our own solar system, there is an important difference. At 70 μm the signal from our Kuiper Belt would be a few percent of the stellar photosphere, while that from our asteroid belt would be less than 0.1% of the stellar photosphere. The dust luminosities inferred for our FEPS sources are several orders of magnitude above these levels. We have argued based on the age distribution of our sample that some of these systems may be younger analogs of our own cold outer dust distribution, but the majority appear to have higher dust levels relative to our evolving solar system.

We can compare our work to analyses of solar-type stars previously detected in the *IRAS* survey and/or in *ISO* pointed observations (e.g., the systematic studies by Mannings & Barlow [1998], Silverstone [2000], and Decin et al. [2003], or the modern reanalyses of data from both space observatories by, e.g., Moór et al. [2006] and Rhee et al. [2007][19]). Comparative plots of $L_{\rm dust}$ versus $T_{\rm dust}$ and $R_{\rm dust}$ versus $T_{\rm dust}$ show that FEPS is finding somewhat warmer, closer in, and slightly lower luminosity disks relative to previous work. Numbering only a few tens before *Spitzer*, the sample of debris disks surrounding *solar-type field stars* has increased by more than fourfold, collating results from various *Spitzer* programs. Approximately 45 of these new debris disk detections come from the FEPS survey of 328 young FGK stars using IRAC, IRS, and MIPS data, as summarized in J. M. Carpenter et al. (2008a, in preparation).

Another large debris disk survey is the MIPS GTO FGK Survey, designed to search for excesses around 150 stars using IRS and MIPS. These targets are generally older and located at smaller distances relative to the FEPS targets. Results presented in Bryden et al. (2006) and Beichman et al. (2006, 2007) indicate a 13% $\pm$ 3% detection rate of 3 σ confidence level emission at 70 μm (derived from 12/88 stars detected plus accounting for the stars with large excesses intentionally left out of the survey). Of the 12 stars with 70 μm excess, most have longer wavelength IRS spectra rising above the photosphere at the red end, and 4 also show weak 24 μm excess, indicating that the dust is located beyond 5–10 AU. We can compare the above with the 6%–10% detection rate of 70 μm excess from the younger but typically more distant (and hence more limited by sensitivity) FEPS sources. There are additional long-wavelength *Spitzer* results within the younger age range of FEPS stars (e.g., Low et al. 2005; Smith et al. 2006; Padgett et al. 2006; Cieza et al. 2007). A complete analysis of dust temperature/location and luminosity versus stellar age may soon be possible.

8. CONCLUDING REMARKS

In the present work we have identified 25 likely and six possible debris disk systems plus six primordial disks based on 70 μm excesses observed with *Spitzer*. In addition to confirming previously known/suspected debris systems, we have newly discovered 14 systems (see Table 1).

Rather than the selection of 70 μm excess sources resulting in physically similar dust belts, we find from simple blackbody

[19] These two papers reach conflicting results on the debris disk status of at least 10 stars.

modeling of the debris systems factors of more than several in the dynamic range of the physical parameters. $T_{\rm dust}$ ranges from 45 to >100 K, $R_{\rm dust,inner}$ from 7 to 90 AU, $f = L_{\rm dust}/L_* $ from $10^{-4.75}$ to $10^{-2.75}$, and $M_{\rm dust}$(minimum) from 10^{-6} to $10^{-2.5}$ $M_\oplus$. We also place limits on the amount of dust in the relatively cleared regions interior to our derived $R_{\rm dust,inner}$, finding $<10^{-6}$ to 10^{-4} $M_\oplus$. We argue for approximately $\frac{1}{3}$ of our systems that extended disk models are more appropriate than single ring models. Such models imply disks with inferred (but poorly constrained) $R_{\rm dust,outer}$ values ranging from 35 to beyond 200. The debris disks are thus factors of several to tens wide in $\delta R/R$, compared to the solar system's two debris belts, which are each only about 50%–75% wide.

The above characteristics suggest that the massive disks we see are collisionally dominated and thus potentially earlier analogs of the present-day solar system's dusty debris system (in which the dynamics is controlled by radiation and mechanical wind effects rather than by collisions, and in which there are massive planets located in the debris-free zones). The large radial extent of the dust implies either wide planetesimal disks as well or multiple narrow planetesimal belts, given the collisional nature of the debris. From our survey of 328 solar-type stars ranging in age from 0.003 to 3 Gyr, at least 6%–10% of solar-type stars appear to have cold debris. We direct the reader to J. M. Carpenter et al. (2008a, in preparation) for discussion of the complete set of cold, warm, and hot debris disks from the FEPS program.

Future investigations of the debris systems identified here will include high spatial resolution imaging in scattered light and thermal emission, in order to determine the dust geometry, particle size distribution, and temperature structure, as well as the application of various planet detection techniques, in order to detect directly the large bodies responsible for inducing the collisional cascade and leading to the dust that we infer from *Spitzer* data. One of our debris systems, HD 38529, is known already to harbor such a planetary system.

Spitzer in general and FEPS in particular are dramatically increasing the sample of nearby cold debris disks. Indeed, this is a "sweet spot" for the *Spitzer Space Telescope*. The new objects are typically fainter in terms of fractional infrared luminosity than those found from studies with previous-generation satellites such as *IRAS* and *ISO*. True analogs to our *inner* solar system debris, with its asteroid belt that is controlled dynamically by massive Jupiter, remain elusive; we are still several orders of magnitude above required observational sensitivity and precision for detection of the current or even earlier (higher) inferred dust levels (including with the state-of-the-art *Spitzer* telescope). However, we have approached the observational sensitivity needed to detect current *outer* solar system dust values, found in the Kuiper Belt region, which is sculpted by Neptune.

Probing effectively the formation and evolution of solar systems within this *Spitzer* Legacy Program, we are even more sensitive to extrapolations backward in time to a younger version of our solar system's cold dust. Based on the architecture of our own solar system, we would not expect to see as much dust at cool temperatures (corresponding to location between the Kuiper Belt and asteroid belt) at any point, even allowing for various planetary orbital migration scenarios (e.g., Bottke et al. 2005; Levison & Morbidelli 2003). That we see a range of dust temperatures and dust luminosities/masses in other debris disk systems may not be too surprising given the diversity of protoplanetary disk properties and planetary architectures found among the known exosolar planet population.

We thank all members of the FEPS team for their contributions to this effort. We also acknowledge with appreciation the long-term contributions of the *Spitzer* instrument teams and *Spitzer* Science Center staff. Our work is based on observations made with the *Spitzer Space Telescope*, which is operated by JPL/Caltech under NASA contract 1407. FEPS is supported through NASA contracts 1224768, 1224634, and 1224566 administered through JPL.

REFERENCES

Ardila, D. R., et al. 2004, ApJ, 617, L147
Artymowicz, P. 1988, ApJ, 335, L79
Backman, D. 2004, in ASP Conf. Ser 324, Debris Disks and the Formation of Planets, ed. L. Caroff et al. (San Francisco: ASP), 9
Backman, D., Dasgupta, A., & Stencel, R. E. 1995, ApJ, 450, L35
Backman, D., & Paresce, F. 1993, in Protostars and Planets III, ed. E. H. Levy & J. I. Lunine (Tucson: Univ. Arizona Press), 1253
Beichman, C. A., Fridlund, M., Traub, W. A., Stapelfeldt, K. R., Quirrenbach, A., & Seager, S. 2007, in Protostars and Planets V, ed. B. Reipurth, D. Jewitt, & K. Keil (Tucson: Univ. Arizona Press), 915
Beichman, C. A., et al. 2006, ApJ, 652, 1674
Bottke, W. F., Durda, D. D., Nesvorny, D., Jedicke, R., Morbidelli, A., Vokrouhlický, D., & Levison, H. F. 2005, Icarus, 179, 63
Bouwman, J., et al. 2008, ApJ, in press
Bryden, G., et al. 2006, ApJ, 636, 1098
Burns, J. A., Lamy, P. L., & Soter, S. 1979, Icarus, 40, 1
Carpenter, J. M., Wolf, S., Schreyer, K., Launhardt, R., & Henning, T. 2005, AJ, 129, 1049
Cieza, L., et al. 2007, ApJ, 667, 308
Cohen, M., Megeath, S. T., Hammersley, P. L., Martiín-Luis, F., & Stauffer, J. 2003a, AJ, 125, 2645
Cohen, M., Wheaton, W., & Megeath, S. T. 2003b, AJ, 126, 1090
Decin, G., Dominik, C., Malfait, K., Mayor, M., & Waelkens, C. 2000, A&A, 357, 533
Decin, G., Dominik, C., Waters, L. B. F. M., & Waelkens, C. 2003, ApJ, 598, 636
Dohnanyi, J. W. 1969, J. Geophys. Res., 74, 2531
Dole, H., Lagache, G., & Puget, J.-L. 2003, ApJ, 585, 617
Dole, H., et al. 2004a, ApJS, 154, 87
———. 2004b, ApJS, 154, 93
Dominik, C., & Decin, G. 2003, ApJ, 598, 626
Downes, A. J. B., Peacock, J. A., Savage, A., & Carrie, D. R. 1986, MNRAS, 218, 31
Dullemond, C. P., Hollenbach, D., Kamp, I., & D'Alessio, P. 2007, in Protostars and Planets V, ed. B. Reipurth, D. Jewitt, & K. Keil (Tucson: Univ. Arizona Press), 555
Durda, D. D., & Dermott, S. F. 1997, Icarus, 130, 140
Fajardo-Acosta, S. B., Stencel, R. E., Backman, D. E., & Thakur, N. 1999, ApJ, 520, 215
Fixsen, D. J., & Dwek, E. 2002, ApJ, 578, 1009
Frayer, D. T., et al. 2006, AJ, 131, 250
Gautier, T. N., et al. 2007, ApJ, 667, 527
Gladman, B., Kavelaars, J. J., Petit, J. M., Morbidelli, A., Holman, M. J., & Loredo, Y. 2001, AJ, 122, 1051
Gordon, K., et al. 2005, PASP, 117, 503
Gregorio-Hetem, J., Lepine, J. R. D., Quast, G. R., Torres, C. A. O., & de La Reza, R. 1992, AJ, 103, 549
Habing, H. J, et al. 2001, A&A, 365, 545
Hines, D. C., et al. 2007, ApJ, 671, L165
Jura, M. 2004, ApJ, 603, 729
Jura, M., Ghez, A. M., White, R. J., McCarthy, D. W., Smith, R. C., & Martin, P. G. 1995, ApJ, 445, 451
Kalas, P., Graham, J. R., Clampin, M. C., & Fitzgerald, M. P. 2006, ApJ, 637, L57
Kenyon, S. J., & Bromley, B. C. 2005, AJ, 130, 269
Kim, J. S., et al. 2005, ApJ, 632, 659
Krivov, A. V., Mann, I., & Krivova, N. A. 2000, A&A, 362, 1127
Landgraf, M., Liou, J.-C., Zook, H., & Grun, E. 2002, AJ, 123, 2857
Levison, H. F., & Morbidelli, A. 2003, Nature, 426, 419
Löhne, T., Krivov, A. V., & Rodmann, J. 2008, ApJ, 673, 1123
Low, F. J., Smith, P. S., Werner, M., Chen, C., Krause, V., Jura, M., & Hines, D. C. 2005, ApJ, 631, 1170

Mamajek, E. E., Meyer, M. R., Hinz, P. M., Hoffmann, W. F., Cohen, M., & Hora, J. L. 2004, ApJ, 612, 496
Mannings, V., & Barlow, M. J. 1998, ApJ, 497, 330
Mathis, J. S., Rumpl, W., & Nordsieck, K. H. 1977, ApJ, 217, 425
Matt, S., & Pudritz, R. E. 2007, in IAU Symp. 243, Star-Disk Interaction in Young Stars, ed. J. Bouvier & I. Appenzeller (Cambridge: Cambridge Univ. Press), 299
Metchev, S., et al. 2008, ApJ, submitted
Metchev, S. A., Hillenbrand, L. A., & Meyer, M. R. 2004, ApJ, 600, 435
Meyer, M. R., Backman, D. E., Weinberger, A. J., & Wyatt, M. C. 2007, in Protostars and Planets V, ed. B. Reipurth, D. Jewitt, & K. Keil (Tucson: Univ. Arizona Press), 573
Meyer, M. R., et al. 2004, ApJS, 154, 422
———. 2006, PASP, 118, 1690
———. 2008, ApJ, 673, L181
Moór, A., Ábrahám, P., Derekas, A., Kiss, C., Kiss, L. L., Apai, D., Grady, C., & Henning, T. 2006, ApJ, 644, 525
Morbidelli, A., Tsiganis, K., Crida, A., Levison, H. F., & Gomes, R. 2007, AJ, 134, 1790
Moro-Martín, A., & Malhotra, R. 2002, AJ, 124, 2305
———. 2003, AJ, 125, 2255
———. 2005, ApJ, 633, 1150
Moro-Martín, A., et al. 2007, ApJ, 668, 1165
Najita, J., & Williams, J. P. 2005, ApJ, 635, 625
Neuhäuser, R., et al. 2000, A&AS, 146, 323
Ozernoy, L. M., Gorkavyi, N. N., Mather, J. C., & Taidakova, T. A. 2000, ApJ, 537, L147
Padgett, D. L., et al. 2006, ApJ, 645, 1283
Papovich, C., et al. 2004, ApJS, 154, 70
Pascucci, I., et al. 2006, ApJ, 651, 1177
———. 2007, ApJ, 663, 383
Patten, B. M., & Willson, L. A. 1991, AJ, 102, 323
Rhee, J. H., Song, I., Zuckerman, B., & McElwain, M. 2007, ApJ, 660, 1556
Rieke, G. H., et al. 2004, ApJS, 154, 25
———. 2005, ApJ, 620, 1010
Silverstone, M. D. 2000, Ph.D. thesis, UCLA
Silverstone, M. D., et al. 2006, ApJ, 639, 1138
Smith, P. S., Hines, D. C., Low, F. J., Gehrz, R. D., Polomski, E. F., & Woodward, C. E. 2006, ApJ, 644, L125
Spangler, C., Sargent, A. I., Silverstone, M. D., Becklin, E. E., & Zuckerman, B. 2001, ApJ, 555, 932
Stapelfeldt, K. R., et al. 2004, ApJS, 154, 458
Stern, S. A. 1996a, A&A, 310, 999
———. 1996b, AJ, 112, 1203
Stern, S. A., & Colwell, J. 1997, ApJ, 490, 879
Su, K. Y. L., et al. 2005, ApJ, 628, 487
Sylvester, R. J., & Mannings, V. 2000, MNRAS, 313, 73
Sylvester, R. J., Skinner, C. J., Barlow, M. J., & Mannings, V. 1996, MNRAS, 279, 915
Teplitz, V., Stern, S., Anderson, J., Rosenbaum, D., Scalise, R., & Wentzler, P. 1999, ApJ, 516, 425
Thébault, P., & Augereau, J.-C. 2007, A&A, 472, 169
Thébault, P., Augereau, J. C., & Beust, H. 2003, A&A, 408, 775
Wahhaj, Z., Koerner, D. W., & Sargent, A. I. 2007, ApJ, 661, 368
Weingartner, J. C., & Draine, B. T. 2001, ApJ, 548, 296
Williams, J. P., Najita, J., Liu, M. C., Bottinelli, S., Carpenter, J. M., Hillenbrand, L. A., Meyer, M. R., & Soderblom, D. R. 2004, ApJ, 604, 414
Wolf, S., & Hillenbrand, L. A. 2003, ApJ, 596, 603
Wood, B. E., Muller, H.-R., Zank, G. P., Linsky, J. L., & Redfield, S. 2005, ApJ, 628, L143
Wyatt, M. C. 2005, A&A, 433, 1007
———. 2006, ApJ, 639, 1153
Wyatt, M. C., Smith, R., Su, K. Y. L., Reike, G. H., Greaves, J. S., Beichman, C. A., & Bryden, G. 2007, ApJ, 663, 365